Icarus 296 (2017) 163–178

Contents lists available at ScienceDirect

Icarus

journal homepage: www.elsevier.com/locate/icarus

Changes in Jupiter's Zonal Wind Profile preceding and during the *Juno* mission

Joshua Tollefson[a,*], Michael H. Wong[b], Imke de Pater[a,b], Amy A. Simon[c], Glenn S. Orton[d], John H. Rogers[e], Sushil K. Atreya[f], Richard G. Cosentino[g], William Januszewski[h], Raúl Morales-Juberías[g], Philip S. Marcus[i]

[a] Department of Earth and Planetary Science, University of California, Berkeley, CA 94720, USA
[b] Department of Astronomy, University of California, Berkeley, CA 94720, USA
[c] NASA Goddard Space Flight Center, Solar System Exploration Division (690.0), 8800 Greenbelt Road, Greenbelt, MD 20771, USA
[d] Jet Propulsion Laboratory/California Institute of Technology, M/S 183-501, 4800 Oak Grove Drive, Pasadena, CA 91109, USA
[e] British Astronomical Association, Burlington House, Piccadilly, London W1J 0DU, U.K.
[f] University of Michigan, Department of Climate and Space Sciences and Engineering, Space Research Building, 2455 Hayward St, Ann Arbor, MI 48109, USA
[g] New Mexico Institute of Mining and Technology, Physics Department, Workman Center 345, 801 Leroy Place, Socorro, NM 87801, USA
[h] Space Telescope Science Institute, Baltimore, MD 21218, USA
[i] Department of Mechanical Engineering, University of California, Berkeley, CA 94720, USA

ARTICLE INFO

Article history:
Received 22 February 2017
Revised 19 May 2017
Accepted 5 June 2017
Available online 7 June 2017

ABSTRACT

We present five epochs of WFC3 HST Jupiter observations taken between 2009–2016 and extract global zonal wind profiles for each epoch. Jupiter's zonal wind field is globally stable throughout these years, but significant variations in certain latitude regions persist. We find that the largest uncertainties in the wind field are due to vortices or hot-spots, and show residual maps which identify the strongest vortex flows. The strongest year-to-year variation in the zonal wind profiles is the 24°N jet peak. Numerous plume outbreaks have been observed in the Northern Temperate Belt and are associated with decreases in the zonal velocity and brightness. We show that the 24°N jet peak velocity and brightness decreased in 2012 and again in late 2016, following outbreaks during these years. Our February 2016 zonal wind profile was the last highly spatially resolved measurement prior to *Juno*'s first science observations. The final 2016 data were taken in conjunction with *Juno*'s perijove 3 pass on 11 December 2016, and show the zonal wind profile following the plume outbreak at 24°N in October 2016.

1. Introduction

The most striking feature of Jupiter is its banded structure, home to swaths of bright, colorful clouds and immense vortices. The observed zonal flow, defined as the longitudinal average of the east-west winds in the visible cloud deck, is one of the most fundamental constraints on the circulation of Jupiter's atmosphere (Ingersoll et al., 2004). Jupiter's zonal wind profile (ZWP) has been a subject of intense study since the Voyager missions. Despite regular derivations of Jupiter's ZWP over the past 30 years, listed in Table 1, the winds have remained remarkably stable, with speeds up to 150 ms^{-1} and with variability on the order of 10 ms^{-1}. In contrast, the clouds of Neptune have displayed evidence of peculiar dynamics ever since Neptune's ZWP was first derived from Voyager 2 data (Limaye and Sromovsky, 1991). In particular, individual bright cloud features on Neptune can move with velocities more than 100 ms^{-1} off the Voyager-derived ZWP (Sromovsky et al., 1993; Martin et al., 2012; Fitzpatrick et al., 2014; Tollefson et al., 2017). What drives Jupiter's stable zonal flow, characterizing the magnitude and timescale of variability (if any) in Jupiter's jet peaks, and predicting how the zonal flow changes with depth remain outstanding questions today.

Three primary methods are used to directly calculate Jupiter's ZWP: 1D correlation, 2D correlation, and discrete feature tracking. In addition, the zonal winds may be indirectly determined by using the thermal wind relationship (Gierasch et al., 1986; Flasar et al., 2004; Simon et al., 2015). 1D correlation methods compute the zonal velocity by calculating longitudinal correlations of the clouds between sets of image pairs in a mosaic, typically in narrow latitude windows, but along a large range of longitudes. This method is insensitive to the north-south component of the velocity field,

* Corresponding author.
E-mail address: jtollefs@berkeley.edu (J. Tollefson).

http://dx.doi.org/10.1016/j.icarus.2017.06.007
0019-1035/

Table 1
Compilation of derived Zonal Wind Profiles for Jupiter. 'Global' describes either the 1D or 2D correlation methods, while 'Local' describes feature tracking.

Timespan (years)	Facility	Appx. Sub-observer Resolution (km/pixel)	Method	References
1979	Voyager 1 & 2 ISS	100	Local	Ingersoll et al. (1981)
			Local	Limaye et al. (1982)
			Global	Limaye (1986)
1995–2000	HST WFPC2	140	Global	García-Melendo and Sánchez-Lavega (2001)
2000	Cassini	120	Global	Porco et al. (2003)
			Local	Li et al. (2004)
			Local	Li et al. (2006)
2007	HST WFPC2	160	Global	Cheng et al. (2008)
2008	HST WFPC2	160	Global	Asay-Davis et al. (2011)
2011	PVOL/IOPW	380	Global	Barrado-Izagirre et al. (2013)
2009–16	HST WFC3	130	Global	This work

but meridional velocities are generally small when intense vortices are absent. The 1D correlation method is favored for its computational efficiency, and it reduces uncertainties due to bad pixels and random errors (Asay-Davis et al., 2011).

The 2D correlation method involves computing full horizontal flow fields, and averaging the east-west components over longitude to obtain the zonal velocity. This method has the advantage that longitudinal variations in the zonal winds are preserved and north-south velocities can be measured in high spatial resolution data. This is particularly important for obtaining accurate zonal wind measurements of the dark projections (associated with the 5 μm hotspots) at 8°N, whose velocities do not move with the true zonal flow at the visible cloud deck (Ortiz et al., 1998; Arregi et al., 2006; García-Melendo et al., 2011; Asay-Davis et al., 2011).

Discrete tracking methods determine zonal velocities by tracking large-scale features over long periods of time to generate one-dimensional or two-dimensional velocity fields. These fields are then averaged over their east-west components to give the mean zonal wind speed in a particular latitude bin.

'Global' correlation methods is an umbrella term to describe both 1D and 2D correlation methods – each utilize correlations at all longitudes of Jupiter. In contrast, feature tracking is often localized to longitude regions containing high-contrast trackable features. In data at low spatial resolution, including even amateur data, global methods can be used by combining results from multiple image pairs (Barrado-Izagirre et al., 2013; Hueso et al., 2017).

Among the past three decades of Jupiter ZWP derivations at the visible cloud deck, minimal wavelength dependence has been found (García-Melendo and Sánchez-Lavega, 2001), in contrast to the case for Saturn (Sánchez-Lavega et al., 2016; Pérez-Hoyos and Sánchez-Lavega, 2006). Images of Jupiter in the ultraviolet have been made to determine zonal wind profiles above the visible cloud deck (Li et al., 2006). Thus, all observations listed in Table 1, with the exception of Li et al. (2006), probe the same cloud vertical levels and any changes in the ZWP reflect temporal changes in Jupiter's atmosphere. Under this assumption, we derive ZWPs to examine changes in the 2009–2016 period, using data acquired with the Wide Field Camera 3 (WFC3) on the Hubble Space Telescope (HST). We use the 1D method to derive ZWPs, but also measure 2D velocity residuals from these mean profiles, preserving information on small vortex circulation, turbulence, and waves. The February 2016 ZWP is the last one measured from high spatial resolution data prior to *Juno*'s first science observations at perijove 1 (PJ1), which took place 27 August 2016 (Bolton et al., 2017). We also present a ZWP taken coincident to perijove 3 (PJ3), which occurred on 11 December 2016.

2. Description of observations

We derive zonal velocities from multiple HST image sets taken with the WFC3 from 2009 to 2016. The sub-observer pixel resolution of these images ranged from ∼ 130 km/pixel at opposition to 170 km/pixel at the PJ3 perijove distance of 5.85 AU. Table 2 gives details of each dataset, including filters, number of images used, and times of each image. We perform analysis on filters at red optical wavelengths to optimize feature contrast. Contrast can be reduced at shorter or longer wavelengths, due to Rayleigh scattering and/or haze reflectivity.

We collected data from four different WFC3 programs. The 2009 dataset was the first global mapping effort with WFC3 after it was installed in Hubble's final servicing mission. At opposition, Jupiter easily fits within a WFC3 2K subarray. Subarrays greatly increase duty cycle efficiency for WFC3 observations, because the instrument buffer can only hold two full frame (4K × 4K) exposures. But instrument modes were limited in WFC3's first observing cycle, so the only way to read out subarrays was to use quad filters (Wong et al., 2010). To increase HST scheduling flexibility, the 2009 observations imaged two hemispheres separately, one on 18–19 September, and the other on 22–23 September (Table 2). Fig. 1 shows a combined map of the two hemispheres, with the derived zonal wind profile overlaid (discussed in the following section).

The 2012 dataset (Fig. 2) was proposed as an attempt to measure a photometric dimming from the shadow of Venus, during a solar transit event as seen from Jupiter. The transit signal itself was never observed, due to the much greater contribution from horizontal inhomogeneity in Jupiter's lightcurve (Karalidi et al., 2015). The choice of a medium bandwidth filter (F763M) to image Jupiter's bright disk necessitated the shortest WFC3/UVIS integration time (0.48 s).[1]

Datasets from 2015 and early 2016 are part of the Outer Planet Atmospheres Legacy (OPAL) program (Simon et al., 2015). This program observes each of the giant planets at an annual cadence, for long-duration time-domain studies of storm activity, wind field variability, and changes in aerosol distributions and spectral properties. The program, which began in 2014, has led to discoveries of a new dark vortex on Neptune (Wong et al., 2016), rare wave phenomena on Jupiter (Simon et al., 2015), and new insights into variable cloud features on Uranus (Wong et al., 2015b; Irwin et al., 2017). The 2015 and 2016 global maps and zonal wind profiles are shown in Figs. 3 and 4 respectively.

The December 2016 dataset is part of the Wide Field Coverage for Juno (WFCJ) program. This program is synchronized with peri-

[1] In short exposures, the WFC3/UVIS shutter introduces an expected variability of about 2% in exposure time (Hilbert, 2009), which should have dwarfed the predicted 0.01% signal (Pasachoff et al., 2013) from the Venus transit. However, the observed lightcurve seemed to be stable against shutter non-repeatability to within 1 part per thousand. This result raises the possibility that the Hilbert (2009) shutter repeatability analysis may have been limited by lower signal-to-noise ratio, compared to the very high signal-to-noise ratio of the Karalidi et al. (2015) Jupiter lightcurve, which integrated the flux over the full planetary disk.

Table 2
The epochs and filters used to derive Jupiter's ZWP in this study.

Data set	Filter	Date	UT Times				
Epoch: 2009.72	FQ643N	09–18	13:13:10	13:16:15	13:31:45	13:55:42	13:58:47
PI: I. de Pater			14:49:40	14:52:45	15:08:13	15:32:07	15:35:12
Proposal ID: 11559			22:49:13	22:52:18	23:01:37	23:04:42	23:32:17
			23:35:22				
		09–19	02:01:02	02:04:07	02:13:26	02:16:31	02:43:36
			02:46:41				
		09–22	11:31:52	11:34:57	11:50:25	12:14:20	12:17:25
			13:07:45	13:10:50	13:26:18	13:50:14	13:53:19
			14:43:39	14:46:44	15:02:12	15:26:08	15:29:13
			21:07:12	21:10:17	21:19:36	21:22:41	21:50:17
			21:53:22				
		09–23	00:18:58	00:22:03	00:31:22	00:34:27	01:02:03
			01:05:08				
Epoch: 2012.72	F763M	09–19	23:43:20	23:50:39	23:57:58		
PI: G. Schneider		09–20	00:05:17	00:23:28	01:19:04	01:26:23	01:33:42
Proposal ID: 13067			01:41:01	01:59:12	02:54:47	03:02:06	03:09:25
			03:16:44	03:34:55	04:30:29	04:37:48	04:45:07
			04:52:26	05:10:37	06:06:13	06:13:32	06:20:51
			06:39:07	06:46:26	07:41:57	07:49:16	07:56:35
			09:17:40	09:24:59	09:32:18	10:53:24	11:00:43
			11:08:02	12:29:08	12:36:27	12:43:46	14:04:51
			14:12:10	14:19:29	14:27:21	15:40:35	15:47:54
			15:55:13	16:02:32	17:16:19	17:23:38	17:30:57
			17:38:16	17:57:00	18:52:02	18:59:21	19:06:40
			19:13:59	19:32:43	20:27:46	20:35:05	20:42:24
			20:49:43	21:07:54			
Epoch: 2015.05	F631N	01–19	02:16:48	02:56:55	03:52:18	04:32:25	05:27:49
PI: A. Simon			06:07:56	07:03:19	07:43:26	08:38:49	09:18:56
Proposal ID: 13937			10:14:19	10:54:26	11:49:50	12:29:57	15:00:50
			15:41:02	16:36:21	17:16:33	18:11:51	18:52:03
			19:47:22	20:27:34	21:22:56	22:03:08	22:58:22
			23:38:34				
Epoch: 2016.11	F631N	02–09	09:41:57	10:07:03	11:17:21	11:42:27	12:53:20
PI: A. Simon			13:18:26	14:28:43	14:53:49	16:04:07	16:29:13
Proposal ID: 14334			17:39:32	18:04:38	19:14:56	19:40:02	20:50:21
			21:15:32	22:25:45	22:50:56		
		02–10	00:01:08	00:26:19	01:36:32	02:01:43	03:11:21
			03:36:32	04:46:45	05:11:56		
Epoch: 2016.95[1]	F631N	12-11	08:01:08	08:24:51	10:50:45	11:35:55	12:26:07
PI: M.H. Wong			13:11:17	14:01:29	14:46:39	15:36:51	16:22:04
Proposal ID: 14661			18:47:00	21:02:21	21:57:44	22:43:03	23:33:07
		12-12	00:18:26	01:11:57	02:52:12	04:42:53	06:29:57
			07:53:12	09:05:55			

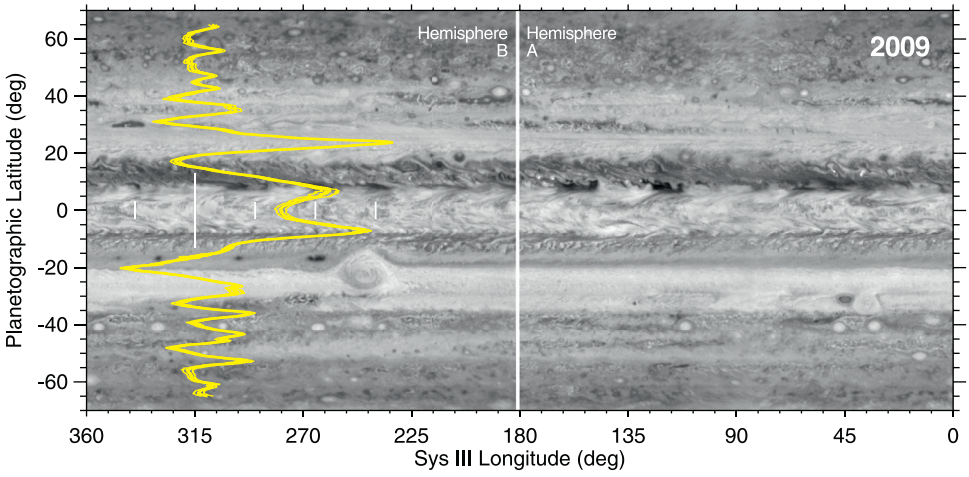

Fig. 1. A global map of Jupiter created by combining frames in the 2009 dataset. Overplotted is the derived ZWP (yellow); thin, white vertical lines are 50 ms^{-1} increments in the zonal wind velocity, with the longest line representing 0 ms^{-1}. Hemispheres A and B (labeled at top) were observed about 4 days apart, with the intention of increasing HST scheduling flexibility (see Section 4.2 and Tables 3 and 4). Subsequent datasets (Figs. 2–5) continuously imaged over full Jupiter rotations, rather than imaging hemispheres separately. (For interpretation of the references to color in this figure legend, the reader is referred to the web version of this article.)

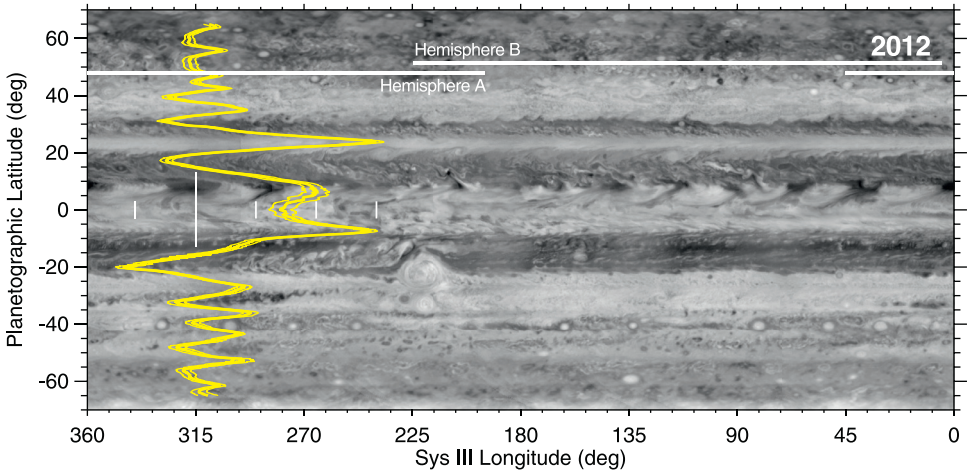

Fig. 2. As Fig. 1. For one analysis (Section 4.2), the data were divided into two hemispheres (marked with horizontal white lines) to determine whether using hemispherical or global imaging influenced the retrieved zonal wind profile.

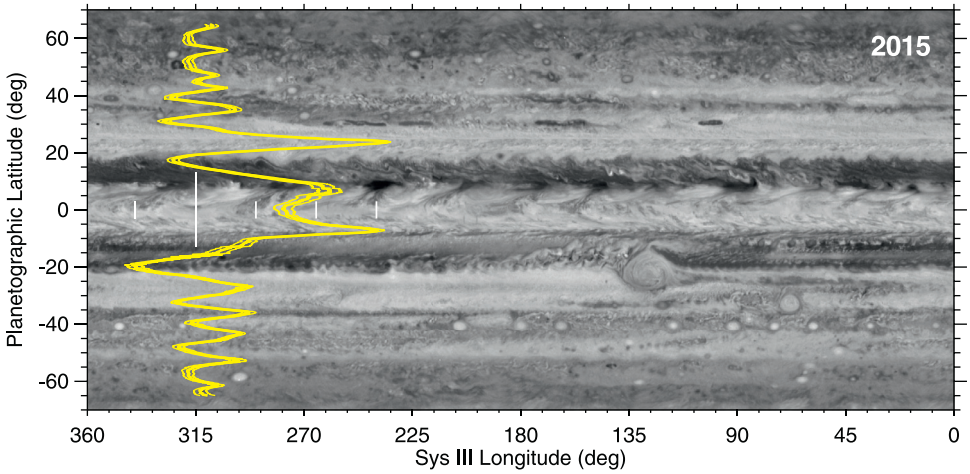

Fig. 3. As Fig. 1 except for 2015.

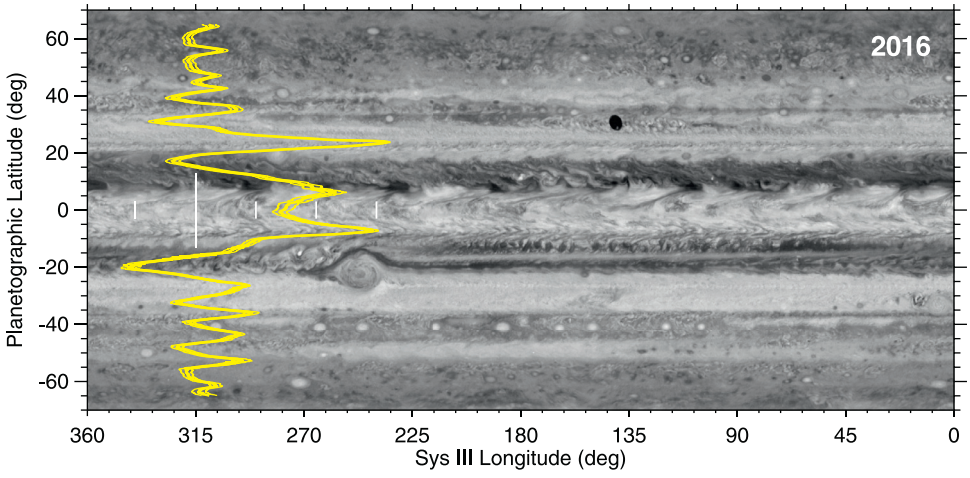

Fig. 4. As Fig. 1 except for 2016.11 (OPAL).

jove passes of the NASA Juno mission. Juno made its third perijove (PJ3) pass on 11 December 2016. For subsequent perijove passes, the WFCJ program will either acquire global map pairs to derive the wind field at the time of perijove, or it will obtain only a ~ 50-min observation covering the longitudes of the Juno sub-spacecraft track. Our global map from the WFJ program is shown in Fig. 5

All images in a given data set were navigated and deprojected using the same methods outlined in Lii et al. (2010). The formal navigational uncertainty for each frame is $\leq 0.10^{\circ}$ at the sub-observer point. Images were deprojected onto a regular grid in planetographic latitude and System-III longitude with 0.05° spacing. Reflectivity data were corrected for limb-darkening by dividing

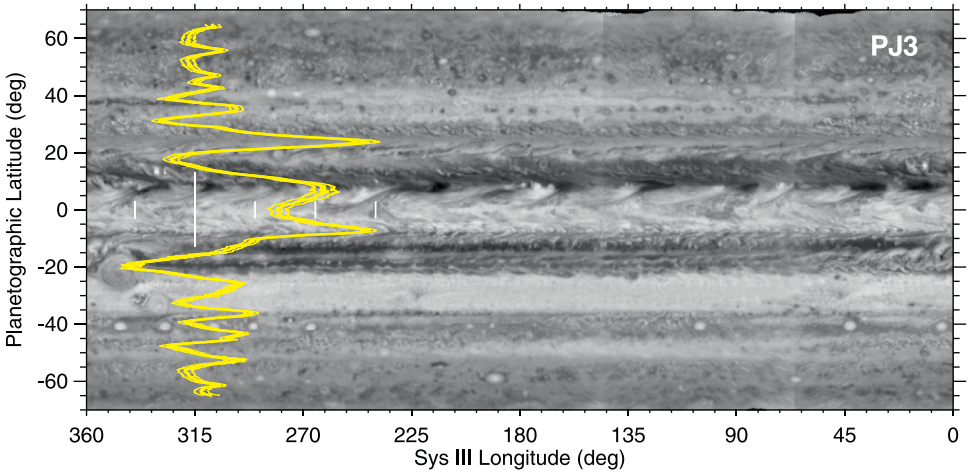

Fig. 5. As Fig. 1 except for 2016.95 (Juno PJ3).

by a factor of μ^k, where μ is the cosine of the emission angle and k ranged from 0.80–0.90 depending on the filter used. For a Lambertian surface, $k = 1.0$. The accuracy of the limb-darkening correction is generally unimportant for our results since we are only interested in correlations in brightness and not exact photometric values – see Supplementary Material for more discussion on the limb-darkening technique.

We also reference results from Cassini maps obtained on 11 to 13 December 2000 during the Jupiter flyby (Porco et al., 2003; Li et al., 2004; Asay-Davis et al., 2011), and from HST/WFPC2 maps from 2008 (Asay-Davis et al., 2011). The HST/WFPC2 maps generally have larger uncertainties in the navigation and zonal wind profiles than the WFC3 maps for several reasons: 1) The WFPC2 pixel scale is slightly larger than the WFC3 pixel scale; 2) Jupiter's full disk did not fit entirely on the PC1 detector resulting in larger navigation uncertainty; 3) the distortion solution may be better for WFC3.

3. Methods

3.1. 1D correlation method for zonal velocity extraction

Our 1D correlation method for zonal velocity extraction is identical to the global method described in Asay-Davis et al. (2011). In summary, maps are sliced into latitude strips, and correlations are derived between pairs of strips as a function of horizontal shift. A given horizontal shift, divided by the time separation of the map strips, is the velocity. Correlations are determined for every point where there is a pair of time-separated maps covering a given longitude. The velocity that maximizes the total correlation is the derived zonal velocity for that latitude bin. This method has advantages over local techniques, where velocities are extracted by tracking features frame-to-frame. Mainly, correlations are computed for all overlapping longitudes in all image pairs. While longitudinal velocity variations are smeared away with the 1D method, the overall error due to random navigation errors and bad pixels is reduced. It is also important to note that there is not necessarily a direct correspondence between the observed cloud motions and the true zonal flow. Features may be driven by a number of mechanisms, including wave phenomena, shear, or local turbulence. Moreover, photometric centers may vary over time due to changes in cloud morphologies. Such processes will affect the uncertainty of our extracted zonal wind profiles. Regardless, we make the assumption that there is a strong correlation between the observed cloud motions and extracted zonal velocities, and show that our mean, global uncertainties are around 5–6 ms^{-1}.

Specifically, we are interested in computing the correlation between a reference image $I_k(\theta, v)$ and an image advected by velocity v to a time in common with the reference, called $I'_k(\theta, v)$, where θ is the planetographic latitude. The velocity that maximizes the correlation function over a sum of all such image pairs in a latitude bin is the derived zonal velocity at the latitude centered in the bin. The correlation function to be maximized used here and by Asay-Davis et al. (2011) is:

$$R(\theta, v) = \sum_{(I_k, I'_k)} \sum_{\theta'=\theta-\Delta\theta}^{\theta+\Delta\theta} \left[\frac{\langle I_k I'_k \rangle - N_{k,k'} \langle I_k \rangle \langle I'_k \rangle}{\sqrt{\left(\langle I_k^2 \rangle - N_{k,k'} \langle I_k \rangle^2\right)\left(\langle I_k'^2 \rangle - N_{k,k'} \langle I'_k \rangle^2\right)}} \right] \quad (1)$$

The function above is dependent on the mean and variance of an image, and the cross-correlation of the unshifted image I_k with the shifted image I'_k. These are defined below:

$$\langle I_k I'_k \rangle(\theta, v) = \frac{1}{N_{k,k'}} \sum I_k(\theta, \phi_i) I'_k(\theta, \phi_i) \quad (2)$$

$$\langle I_k \rangle(\theta, v) = \frac{1}{N_{k,k'}} \sum I_k(\theta, \phi_i) \quad (3)$$

$$\langle I_k^2 \rangle(\theta, v) = \frac{1}{N_{k,k'}} \sum I_k^2(\theta, \phi_i) \quad (4)$$

These quantities sum over $N_{j,\,k}$, which is the number of overlapping pixels between image the pair of images I_j and I'_k at a given θ and v.

To compute the above correlations, we first crop each individual map to ± 40° longitude of the central meridian and ± 72° latitude to limit effects near the limb. We then mask out the Great Red Spot and Oval BA in images where these features are present. Large vortices do not move with the background flow on Jupiter, and have internal velocities that would interfere with our accurate measurement of zonal velocities. This chosen masking is, admittedly, arbitrary. Future implementations may improve on this by first calculating all the residuals from the unmasked data with ACCIV (see Section 3.2), then using the data themselves to flag significant non-zonal flows, and finally re-running the analysis with all areas masked out where the residuals are flagged for exceeding a set threshold. This process would be more time-consuming, but it should reduce the global mean uncertainty.

We also limit our computations to pairs of images that are taken within 5–15 h of each other, corresponding to 0.5–1.5 Jupiter rotations. If the time difference between images is too short, the correlation given in (1) will be large for the sampled velocities since the displacements in the advected image will remain close to the reference image. Too long a time offset and correlations will be small at all sampled velocities, as inherent morphological changes arise and displacements from non-zonal velocities grow. Correlations are computed for velocities within ± 50 ms^{-1} in 0.5 ms^{-1} intervals of a reference zonal wind profile, taken from Cassini maps published in Porco et al. (2003). Finally, we compute (1) by summing over all latitudes within ± $\Delta\theta$ of the given latitude θ. For our zonal velocities, $\Delta\theta = 0.25^{\circ}$ which amounts to summing over 11 rows of pixels, five on either side of the given latitude. Summing over multiple latitudes eliminates correlations produced by spurious and prominent structures at any single latitude, producing a 'smooth' zonal wind profile. This latitude-summing procedure and reference zonal wind profile are identical to that used in Asay-Davis et al. (2011).

3.2. Uncertainties

Uncertainties in some previous works have made use of temporal fluctuations (Limaye, 1986; 1989; García-Melendo and Sánchez-Lavega, 2001). Specifically, when multiple zonal wind profiles can be derived from data taken close in time, the RMS temporal variation among the profiles was taken as the estimate of the uncertainty in the mean profile. RMS differences between profiles contain differences due to both random errors as well as systematic errors, including temporal evolution on the timescale of the separation between individual profiles. But since a major motivation for determining uncertainties is to be able to quantify real temporal change, it would be beneficial to define uncertainties that are independent of temporal variation.

To estimate the precision of our derived zonal wind profiles, we use correlation uncertainties, as defined in Asay-Davis et al. (2011). The error estimation involves first advecting individual maps to a common time point, using the derived zonal wind profile from the 1D method. If the derived profile were perfectly accurate, then these advected maps would all be identical. In reality, the advected maps differ, due to a combination of effects: scale differences between discrete features and jet widths, temporal evolution of cloud tracers, random and periodic longitudinal departures from zonal flow, meridional flow, temporal variation on short timescales, vertical wind shear, noise in image data, navigation errors in mapping the data, and astrometric distortion of the images. The combined effect of these error terms can then be estimated by measuring the displacements between the individual advected maps. We measure displacements using Correlation Image Velocimetry, or CIV (Fincham and Spedding, 1997; Fincham and Delerce, 2000). Displacements are then converted to velocities by dividing by the interval between advected maps. The specific implementation of CIV employed was the ACCIV code, described in Asay-Davis et al. (2011), which includes a statistical filter for rejecting outliers in the velocity field.[2]

The velocity vectors found by correlating advected maps are residuals from the mean flow. We combine and smooth velocity residual vectors from all map pairs to create residual maps. These maps constrain the velocity uncertainty. We define zonal wind profile uncertainty at a given latitude as the RMS average of the velocity residuals at that latitude. Residual maps also reveal dynamical features such as vortices, turbulence, and waves. Correlations cannot be accurately measured at the edges of the maps, which we arbitrarily restricted to latitudes closer than 72° from the equator to limit the effects of viewing geometry distortion and loss of contrast due to greater slant path through Jupiter's hazes.

Uncertainties in the zonal wind profiles are shown as thin yellow lines in Figs. 1–5. Tabular text files containing each zonal wind profile from this paper (with uncertainties) are available in the online article Supplementary Material. The supplementary files also list the number of 2D correlations found at each latitude as part of the uncertainty estimate; very few 2D correlations were found at latitudes north of 69.1°N or south of 69.1°S. Velocity residuals are shown in Fig. 6 for the 2016.11 data set. Residual plots for the other data sets are available in the online Supplementary Materials Figs. S1–S4. The middle panel of each subfigure shows north-south velocity residuals, while the lower panel shows east-west residuals. The top panel shows all residuals overlaid on the global albedo map, with the zonal wind profile shown for comparison at top right. We identify two sources of error that may contribute to the residuals. First is navigational uncertainties, which we estimate as around 0.10° per frame. The second is errors that arise from the correlation calculation. This source of uncertainty is partitioned into: the dynamics of discrete features, like vortices, that drift with respect to the zonal flow; variations in velocity with longitude; variations in velocity with latitude, including deviations within the 11 pixel window as well as North-South velocities; and the effects of limb-darkening. It is harder to determine the magnitude of each of these sources. Fig. 6 shows compact dipoles (pairs of red/blue or orange/blue velocity residuals) which are characteristic of vortices. The presence of these velocity signatures at a particular latitude will increase the standard deviation of velocities at that latitude, so vortices affect the zonal wind uncertainties. For example, a series of cyclonic vortex signatures between 50°–60°S (labeled "Cyclone Alley" in Fig. 6) produces locally high zonal wind uncertainties, as discussed in Section 5.2.

High-Level Science Products (HLSP) are also available at the MAST archive hosted by Space Telescope Science Institute. Calibrated global maps associated with the OPAL program are available at the OPAL HLSP page.[3] Calibrated global maps and zonal wind profiles associated with the WFCJ program, synchronized with Juno perijove passes, will be available at the WFCJ HLSP page.[4] All zonal wind profiles at the WFCJ HLSP page will be derived using the procedures described here, and global maps will be constructed as described in Simon et al. (2015).

4. Results

In the following section we plot our derived zonal wind profiles and compare differences between pairs of profiles. We define the uncertainty in the zonal velocity difference between two profiles at a particular latitude as:

$$RMS_{\text{Total}} = \sqrt{RMS_1^2 + RMS_2^2} \tag{5}$$

RMS_1 and RMS_2 are the correlation velocity uncertainties defined in the previous section. Differences greater than RMS_{Total} are significant. Comparisons between a number of derived ZWPs are presented in Figs. 7–8. For each comparison, two ZWPs are plotted against each other on the left (blue and green curves in the online version of this article), with differences between them shown on the right as a black curve, bounded by the uncertainty envelope in red. Fig. 7 compares zonal wind profiles at multiple epochs, while Figs. 8 and 9 are used to evaluate the effects of differences in our methodology (see below).

[2] ACCIV is available online at https://github.com/xylar/acciv.

[3] The OPAL archive page at MAST has the DOI 10.17909/T9G593, and can be accessed at http://archive.stsci.edu/prepds/opal/.

[4] The WFCJ archive page at MAST can be accessed at http://archive.stsci.edu/prepds/wfcj/.

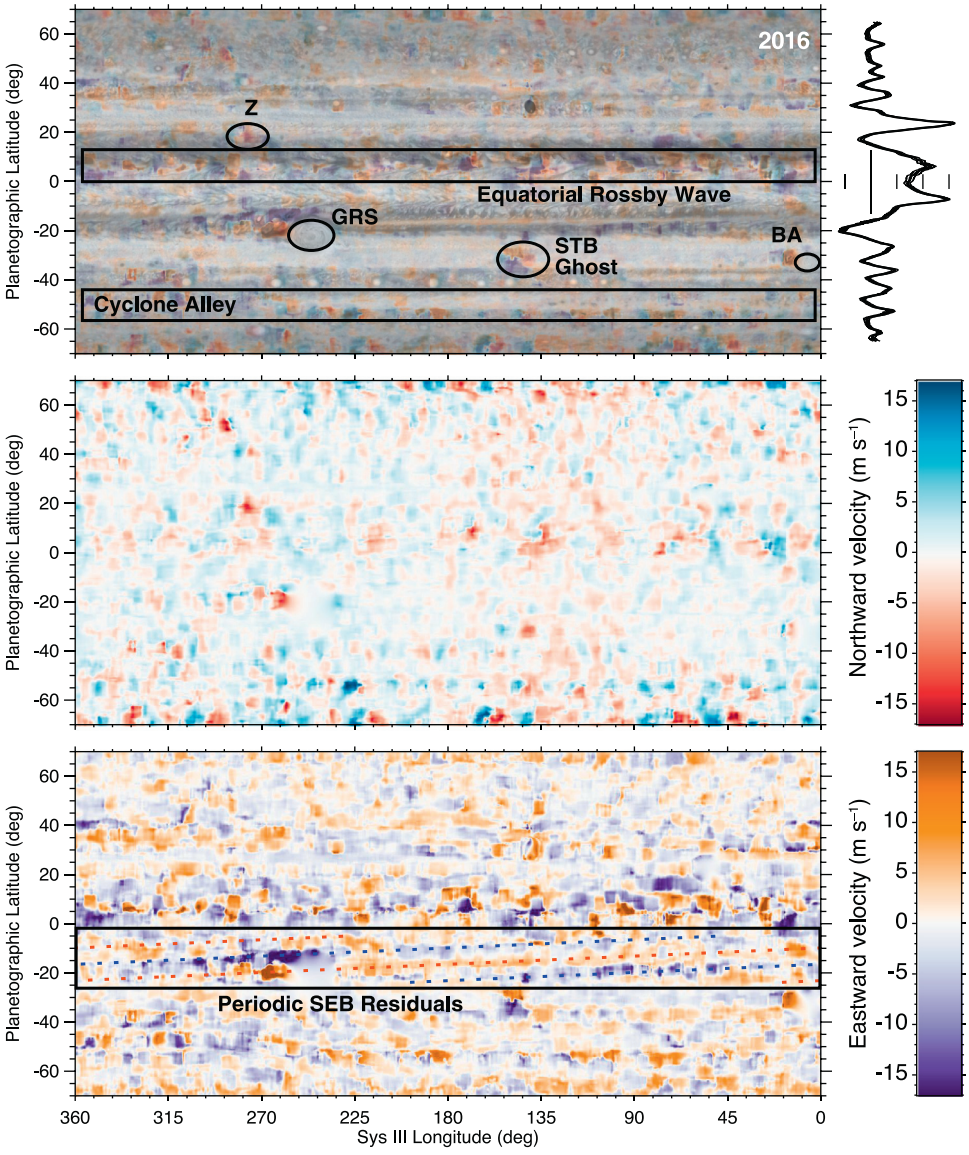

Fig. 6. Residual non-zonal velocities are used to calculate uncertainties, but they also highlight dynamical features. Top panel: All velocity residuals are overlaid on the 2016.11 albedo map from Fig. 4. The GRS and Oval BA were masked out of the 2D correlation retrieval, so their areas are blank. The smaller anticyclone Oval Z, as well as a cyclone known as the STB Ghost are clearly visible in the residual maps. A band near 55°S is marked by strong velocity residuals; we mark this as "Cyclone Alley." Residuals are also very high near 9°N, where an equatorially-trapped Rossby wave produces a series of 5-μm hot spots and plumes. Middle panel: Meridional velocity residuals are shown on their own. Vortices indicated in the top panel show up here as east-west dipoles. Bottom panel: Zonal velocity residuals are shown on their own. Vortices indicated in the top panel show up here as north-south dipoles. A periodic pattern of alternating residuals is seen between the equator and 20°S, with zonal wavenumber 1 (red and blue dotted lines are overplotted as guides to the eye). Residual maps for the other epochs are available in the Supplemental Materials. Similar phenomena are seen on these maps. (For interpretation of the references to color in this figure legend, the reader is referred to the web version of this article.)

4.1. Temporal change

Fig. 7 shows comparisons of the 2016.11 mean ZWP to the mean ZWP's for each other data set (here,'mean' is the average zonal wind speed over all longitudes and frames, in contrast to the other two sets below). The most significant differences in the jet peak speeds occur around 24°N, 8°N, 6°S, 26°S, and 50°S. The zonal wind differences and uncertainties, averaged over ± 65°, are shown in Table 3. We also include the 2008 ZWP from HST/WFPC2 data (Asay-Davis et al., 2011) for comparison. On a global basis, the zonal winds are constant ($\langle\Delta\rangle < \langle\sigma\rangle$), but the few significant changes are highly interesting. We define $\langle\sigma\rangle$ as the globally averaged uncertainty between two epochs, equal to the latitudinal-average RMS_{Total} and $\langle\Delta\rangle$ as the globally averaged difference in the zonal winds in two epochs.

WFC3 provides an improvement in velocity measurement precision compared to WFPC2. Diagonal elements of Table 3 give the uncertainties of each individual ZWP. Average uncertainties measured with WFC3 (years 2009–2016) are considerably lower than the 11 ms^{-1} reported in Asay-Davis et al. (2011) for 2008, based on WFPC2 data. Several instrument-related differences between WFPC2 and WFC3 can be linked to the improvement. WFC3 provides a detector format that allows the full disk of Jupiter to be imaged in every frame, leading to better navigation accuracy than WFPC2, where the high-resolution PC1 chip was too small to capture the full disk. There may be a small improvement due to angular resolution, since the 0.039″ pixel size of WFC3 is a 15% improvement over the 0.046″ WFPC2 pixel size (McMaster et al., 2008). A significant improvement can be seen between uncertainties in 2009 (7.6 ms^{-1}), compared to uncertainties at the later

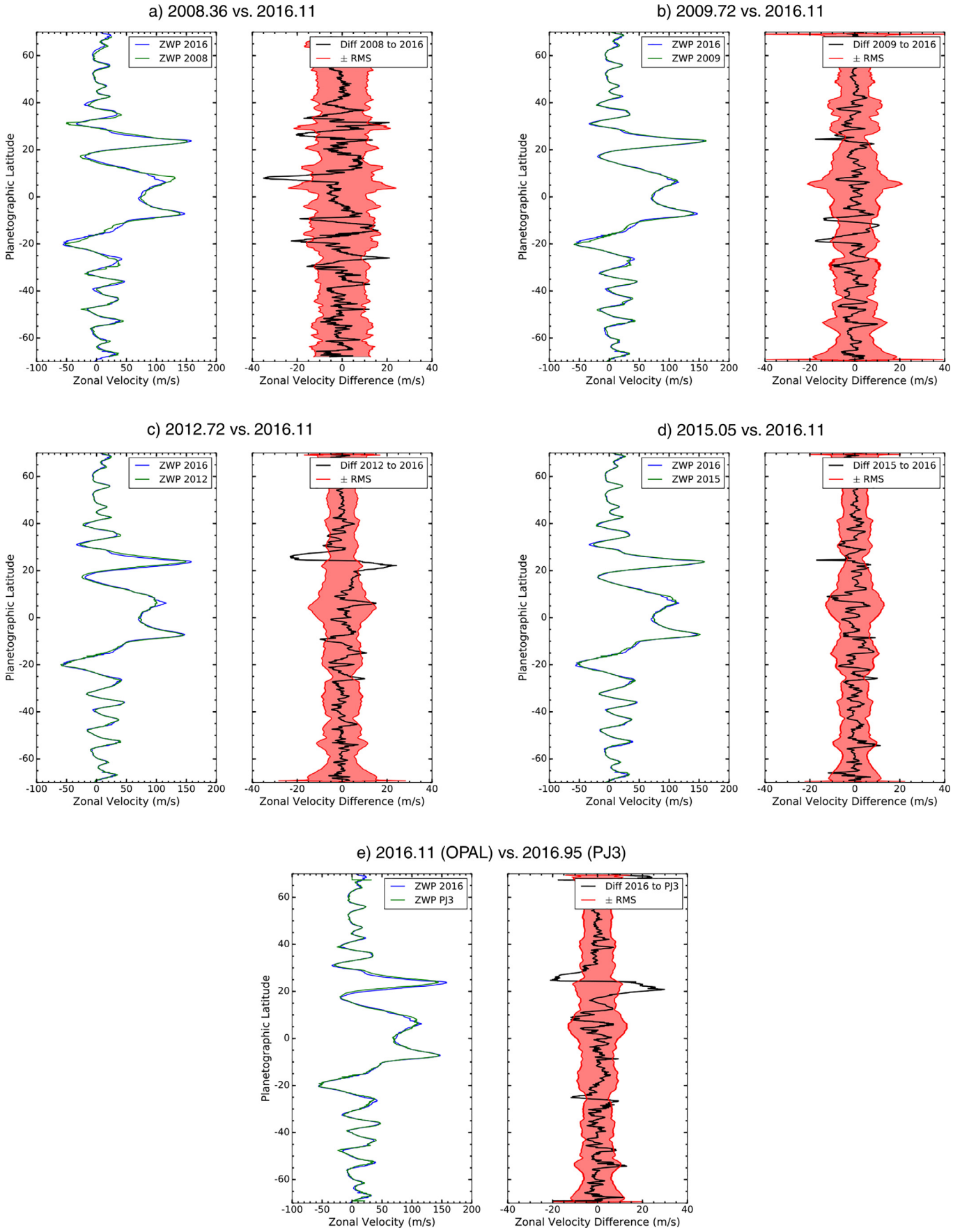

Fig. 7. Left: Jupiter's derived ZWP from 2008–2016 compared to the 2016.11 ZWP. Right: The difference between the compared ZWPs (black line) and RMS Total (Eq. (5), red area). Differences outside the red region are significant. In all figures, the black line is the 2016.11 ZWP minus the ZWP of the compared epoch. (For interpretation of the references to color in this figure legend, the reader is referred to the web version of this article.)

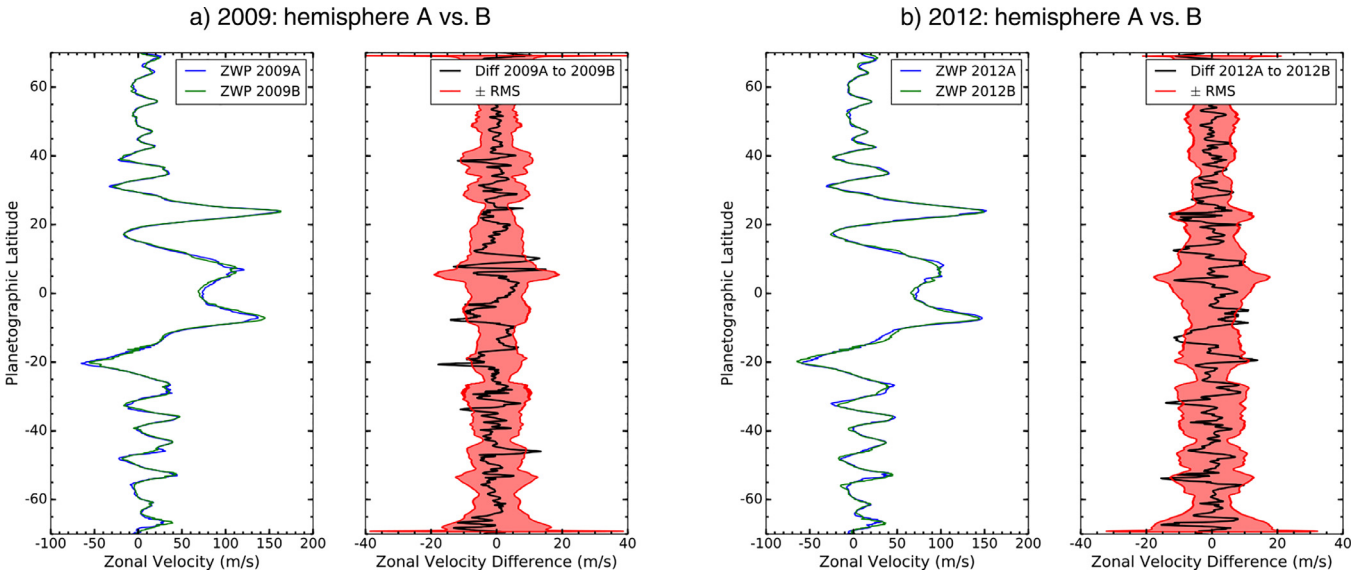

Fig. 8. As Fig. 7 except comparing Hemispheres A and B in the 2009 and 2012 epochs.

Table 3
Year-to-year comparisons of the mean ZWPs. $\langle\sigma\rangle$ is the average uncertainty, equal to the latitudinal-average RMS_{Total} if the comparison is between two different years (values off the main diagonal). Along the diagonal, the reported $\langle\sigma\rangle$ is the average uncertainty for that year (equal to RMS_1). Similarly, $\langle\Delta\rangle$ is the average difference between two years. The units are ms^{-1}.

Year	2016.95	2016.11	2015	2012	2009	2008
2016.95	$\langle\sigma\rangle = 5.7$	$\langle\Delta\rangle = 3.6$ $\langle\sigma\rangle = 7.6$	$\langle\Delta\rangle = 3.6$ $\langle\sigma\rangle = 7.6$	$\langle\Delta\rangle = 3.2$ $\langle\sigma\rangle = 8.2$	$\langle\Delta\rangle = 4.1$ $\langle\sigma\rangle = 9.5$	$\langle\Delta\rangle = 5.9$ $\langle\sigma\rangle = 12.7$
2016.11		$\langle\sigma\rangle = 4.9$	$\langle\Delta\rangle = 2.3$ $\langle\sigma\rangle = 7.0$	$\langle\Delta\rangle = 3.3$ $\langle\sigma\rangle = 7.6$	$\langle\Delta\rangle = 2.9$ $\langle\sigma\rangle = 9.1$	$\langle\Delta\rangle = 5.1$ $\langle\sigma\rangle = 12.3$
2015			$\langle\sigma\rangle = 5.0$	$\langle\Delta\rangle = 3.2$ $\langle\sigma\rangle = 7.7$	$\langle\Delta\rangle = 2.9$ $\langle\sigma\rangle = 9.2$	$\langle\Delta\rangle = 4.9$ $\langle\sigma\rangle = 12.3$
2012				$\langle\sigma\rangle = 5.8$	$\langle\Delta\rangle = 3.5$ $\langle\sigma\rangle = 9.7$	$\langle\Delta\rangle = 5.1$ $\langle\sigma\rangle = 12.7$
2009					$\langle\sigma\rangle = 7.6$	$\langle\Delta\rangle = 4.4$ $\langle\sigma\rangle = 13.6$
2008						$\langle\sigma\rangle = 11.2$

2012, 2015, and 2016.11 epochs (5–6 ms^{-1}). All of these epochs had comparable spatial resolution. This improvement in uncertainties is partially due to improved knowledge of WFC3's geometric distortion, which is corrected to a precision of about 0.001″ (Kozhurina-Platais, 2014). The 2009 data were acquired using the quad filter FQ643N, which (unlike the full-frame filters used in 2012–2016) never received updates to its distortion corrections.

Fig. 7 compares the resulting ZWPs for each epoch. We find significant temporal variability near latitudes of 24°N, 8°N, 6°S, 26°S, and 50°S. Many of these variable regions correspond to non-zonal flow, such as regions with large vortices and the 5-μm hot spots. While we mask out the Great Red Spot, global waves emitting from this vortex still affect the flow. This is reasonable, since the activity of vortices and the dark projections varies with longitude, and we expect these signatures to appear in the ZWP derivations.

The latitude with the greatest uncertainties (widest part of the red envelope) falls in the region of the 8°N 5-μm hot spots. Zonal velocities are notoriously difficult to obtain in this area since the hot spots do not move with the local flow (Ortiz et al., 1998; García-Melendo et al., 2011; Asay-Davis et al., 2011; Choi et al., 2013). Asay-Davis et al. (2011) manually tracked this area and found large RMS deviations. This is suggestive of wave activity or changes in the cloud optical depth, indicative of vertical wind shear. Results from global method analyses are difficult to interpret due to these local variations. The large velocity residuals here are marked "Equatorial Rossby Wave" in Fig. 6.

4.2. Effect of restricted longitude range

The 2009 observations were taken with two hemispheres observed about 4 days apart, in an attempt to increase HST scheduling flexibility. To investigate whether this observation design affected the resulting ZWP, we performed an analysis of the 2012 data in a similar fashion, constructing two different ZWPs from separated hemispheres. The two hemispheres for 2009 are shown in Fig. 1, and for 2012, horizontal bars in Fig. 2 show the longitude ranges used for each separate hemisphere analysis.

Fig. 8a compares differences in the zonal winds between hemispheres A and B in 2009, and Fig. 8b compares the two 2012 hemisphere profiles. Very few significant differences (black curves protruding from red envelopes) are seen at either epoch. In the 2012 dataset, there is a significant difference in the location of the "kink" in the cyclonic shear zone near 15°S, and at both epochs, there are differences in the peak of the strongest westward jet at 20°S (see also Section 5.3).

Table 4 summarizes the latitude-averaged results from the two-hemisphere analyses. As with Table 3, the diagonal of the table gives mean correlation uncertainties $\langle\sigma\rangle$ for each individual ZWP measurement. Uncertainties from all WFC3 analyses, whether global or single-hemisphere, all fall in the 5–6 ms^{-1} range. Differences between 2009A/2009B profiles, and between 2012A/2012B profiles are in the 3 ms^{-1} range, just like the differences between global profiles in 2009, 2012, 2015, and 2016 (Table 3). These re-

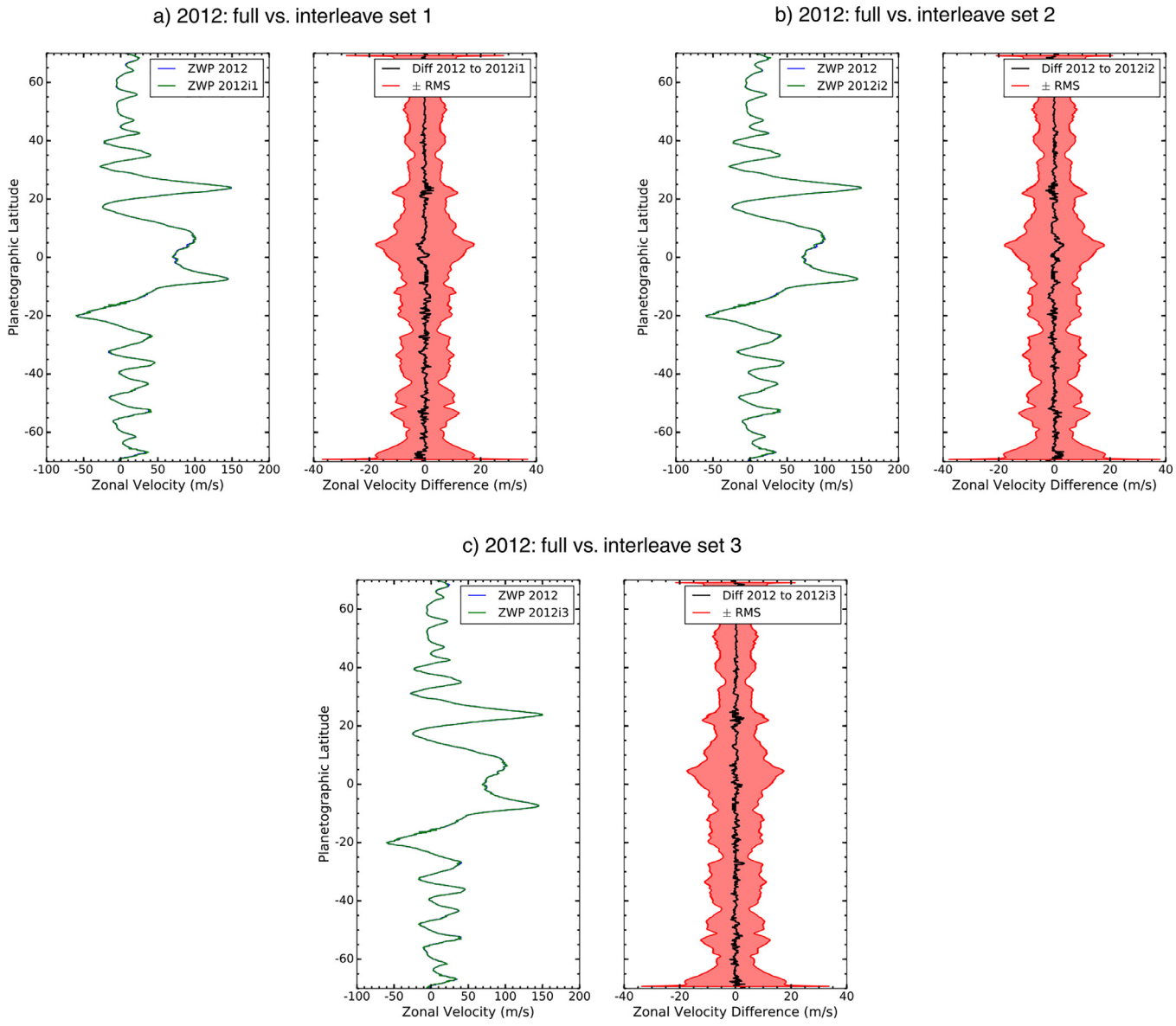

Fig. 9. As Fig. 7 except comparing the interleaved 2012 sets.

Table 4
As Table 3, except comparing the 2009 and 2012 averaged ZWPs with those derived from the individual hemispheres A and B (defined in Fig. 1 and 2).

Year	2012	2012A	2012B	2009	2009A	2009B
2012	$\langle\sigma\rangle = 5.8$	$\langle\Delta\rangle = 1.9$ $\langle\sigma\rangle = 8.4$	$\langle\Delta\rangle = 1.7$ $\langle\sigma\rangle = 7.7$	$\langle\Delta\rangle = 3.5$ $\langle\sigma\rangle = 9.7$		
2012A		$\langle\sigma\rangle = 6.1$	$\langle\Delta\rangle = 3.1$ $\langle\sigma\rangle = 8.0$			
2012B			$\langle\sigma\rangle = 5.0$			
2009				$\langle\sigma\rangle = 7.6$	$\langle\Delta\rangle = 1.5$ $\langle\sigma\rangle = 9.4$	$\langle\Delta\rangle = 1.5$ $\langle\sigma\rangle = 9.3$
2009A					$\langle\sigma\rangle = 5.4$	$\langle\Delta\rangle = 2.9$ $\langle\sigma\rangle = 7.6$
2009B						$\langle\sigma\rangle = 5.1$

sults suggest that a ZWP derived from data covering a single hemisphere may be just as accurate as results from data with full global coverage. Surprisingly, Table 4 suggests that precision is also not decreased by using hemispherical rather than global data: $\langle\sigma\rangle_{2012B} < \langle\sigma\rangle_{2012global} < \langle\sigma\rangle_{2012A}$, and $\langle\sigma\rangle_{2009global}$ is greater than either $\langle\sigma\rangle_{2009A}$ or $\langle\sigma\rangle_{2009B}$. The comparison between these hemispherical and global uncertainties gives some insight into the length scale of longitudinally variable flow; the variation is most likely dominated by length scales significantly shorter than a hemisphere. Indeed, studies of the OPAL 2015 and 2016 data focused on longitudinal variation (Johnson et al., 2017) identified longitudinal variation with horizontal scales of around 50°, based on wind profiles

Table 5
As Table 3, except comparing the 2012 averaged ZWP with each individual interleaved set (i1,i2,i3).

Year	2012	2012i1	2012i2	2012i3
2012	$\langle\sigma\rangle = 5.8$	$\langle\Delta\rangle = 0.5$ $\langle\sigma\rangle = 8.1$	$\langle\Delta\rangle = 0.5$ $\langle\sigma\rangle = 8.1$	$\langle\Delta\rangle = 0.5$ $\langle\sigma\rangle = 8.2$
2012i1		$\langle\sigma\rangle = 5.6$	$\langle\Delta\rangle = 0.9$ $\langle\sigma\rangle = 8.0$	$\langle\Delta\rangle = 0.8$ $\langle\sigma\rangle = 8.1$
2012i2			$\langle\sigma\rangle = 5.6$	$\langle\Delta\rangle = 0.8$ $\langle\sigma\rangle = 8.1$
2012i3				$\langle\sigma\rangle = 5.8$

based on data spanning only 30° of longitude, even shorter than our hemispherical (180°) tests.

4.3. Effect of sampling cadence

Enough individual frames were obtained in 2012 to compare the 'mean' retrieval to retrievals based on interleaved subsets of the data. The interleaved subsets were obtained by taking every third frame from the 2012 data set, resulting in timing differences on the order of 10 min (see Table 2). Each subset had 20 frames, roughly comparable to the number of frames used in the 2015 and 2016 analyses. These interleaved 2012 subsets span the same longitudinal and temporal range, allowing effects on the ZWP due to instrumental or navigational errors to be isolated.

Fig. 9 compares the mean 2012 profile to each interleaved set. The zonal wind differences are small, < 5 ms^{-1} over the full latitude range, and < 1 ms^{-1} in the globally-averaged sense (Table 5). Due to very similar longitudinal and temporal coverage of these three interleaved datasets, differences in the ZWPs should be due only to random errors from sources such as navigation uncertainty or detector distortion. Values of mean ZWP differences $\langle\Delta\rangle <$ 1 ms^{-1} imply that such random errors are very small compared to other uncertainty terms.

Comparisons between the full retrievals, single-hemisphere retrievals, and interleaved 2012 subset retrievals suggest that the dominant error in ZWP measurements is longitudinal variability. Because the 2012 interleaved data sets span the same range of longitudes, they are not sensitive to this source of error, and their differences are smaller than 1 ms^{-1} on average. But the length scale of this longitudinal variability must be shorter than 180°, because there is no significant increase in $\langle\sigma\rangle$ between the 2012 hemispherical and global ZWPs.

Some constraints can also be placed on temporal variation. Differences and uncertainties between 2012A and 2012B retrievals, which were observed within the same 24-h span, are very similar in magnitude to the differences in 2009A and 2009B retrievals, which were taken about 4 days apart. If temporal variability on the scale of 100 h were significant, then the 2009 and 2012 dual-hemisphere results should show some significant differences, perhaps including significantly higher uncertainties or differences in the 2009A/2009B case.

The mean correlation uncertainty is higher for the full 2009 profile ($\langle\sigma\rangle = 7.63$ ms^{-1}) than for the full 2012 profile (5.79 ms^{-1}). However, $\langle\sigma\rangle$ is in the range of 5–6 ms^{-1} for all the single-hemisphere cases. If the difference between the 2009 and 2012 $\langle\sigma\rangle$ values is entirely due to real physical effects, then it suggests a timescale of variation that is on the order of a few days, but long enough to go undetected in the 2012 data spanning only a couple of Jupiter rotations. A caveat to this finding is that there was a potentially significant difference in how the mean 2009 and 2012 profiles were constructed. For 2012, we constructed a mean profile based on global data. For 2009, this approach was impossible because correlations are unreliable over a time span of 4 days, so we averaged the ZWPs from the A and B hemispheres.

5. Discussion

5.1. Periodogram analysis

We added the WFC3 ZWPs to the set of WFPC2 and Voyager profiles analyzed in Simon-Miller and Gierasch (2010), updating the Lomb-Scargle periodogram analysis (Fig. 10). The combined dataset allows a much finer temporal resolution in short (< 8 year) periods. The current analysis combines prior ZWPs derived using a discrete feature tracking (local) method, with the WFC3 ZWPs derived using the 1D correlation (global) method. After more WFC3 zonal wind profiles are measured in the future, there will be sufficient data to determine whether combining data based on different retrieval methods affects the results. However, where the false alarm probability is low, several latitudes show signs of periodic variation, similar to those in Simon-Miller and Gierasch (2010):

Within a few degrees of the equator, variation is suggested with a period of 6.7 years, and possibly at the longest period of 13.8 years. Similar signals were evident in the analyses of Simon-Miller and Gierasch (2010) and Simon-Miller et al. (2007), though with lower confidence; the data used in Simon-Miller et al. (2007) did not have enough temporal coverage to accurately constrain periods. The long-period equatorial variability is intriguingly close to the 11.9-year seasonal period. Because of the nature of the Lomb-Scargle periodogram retrieval, the long period signals have underestimated false alarm probabilities, as there are not yet enough datasets to demonstrate repeatability at the longest timescale. However, the 6.7-year period could correspond to the first overtone of the seasonal frequency. As shown in Fig. 8 of Simon-Miller and Gierasch (2010), there is some indication that tropospheric mesoscale wave features could be tied to the seasonal cycle, and if so, similar changes might be expected in the tropospheric winds.

Peaks also appear at 5 years at 18°N and 7°S, as Simon-Miller and Gierasch (2010). Stratospheric temperatures derived from infrared observations show a strong low-latitude periodicity at about 4.5 years, known as the Quasi-Quadrennial Oscillation (QQO), which should produce observable signals in the tropospheric zonal wind speeds if resulting temperature anomalies propagate down to the cloud tops (e.g. Leovy et al., 1991; Simon-Miller et al., 2007). However, the only periodogram peaks near this period are tightly focused in latitude at 18°N and 7°S, and could be tied to other features, such as the wave pattern at 7°S. The analogous equatorial oscillation in the Earths atmosphere, the Quasi-Biennial Oscillation (QBO), varies from 20 to 26 months, and sometimes fails to fully form at lower altitudes, or pauses. In other words, the Earths QBO is not exactly periodic and does not always fully propagate, so it is possible that the approximately 7-year wind variability seen at Jupiter's equator is also related to this cycle. The best option for distinguishing between these possibilities is the expansion of the regular WFC3 zonal wind time series, which should more accurately determine whether a seasonal signal or equatorial oscillation is present or not; these can be much more tightly constrained with this combined dataset, compared with prior analyses.

There is no significant periodicity at the latitude of 24°N, where the highest-magnitude wind speed changes are found. This point is discussed further in Section 5.3.

5.2. Non-zonal features in the velocity residual maps

The 1D correlation method determines the average zonal flow in Jupiter's atmosphere. This method provides no direct information about flows different of this background. The residuals in Fig. 6 indicate compact dipoles in north-south and east-west velocities where vortices are present in the 2016.11 data. Residual maps for the other epochs (Supplemental Materials) show similar vortex signatures.

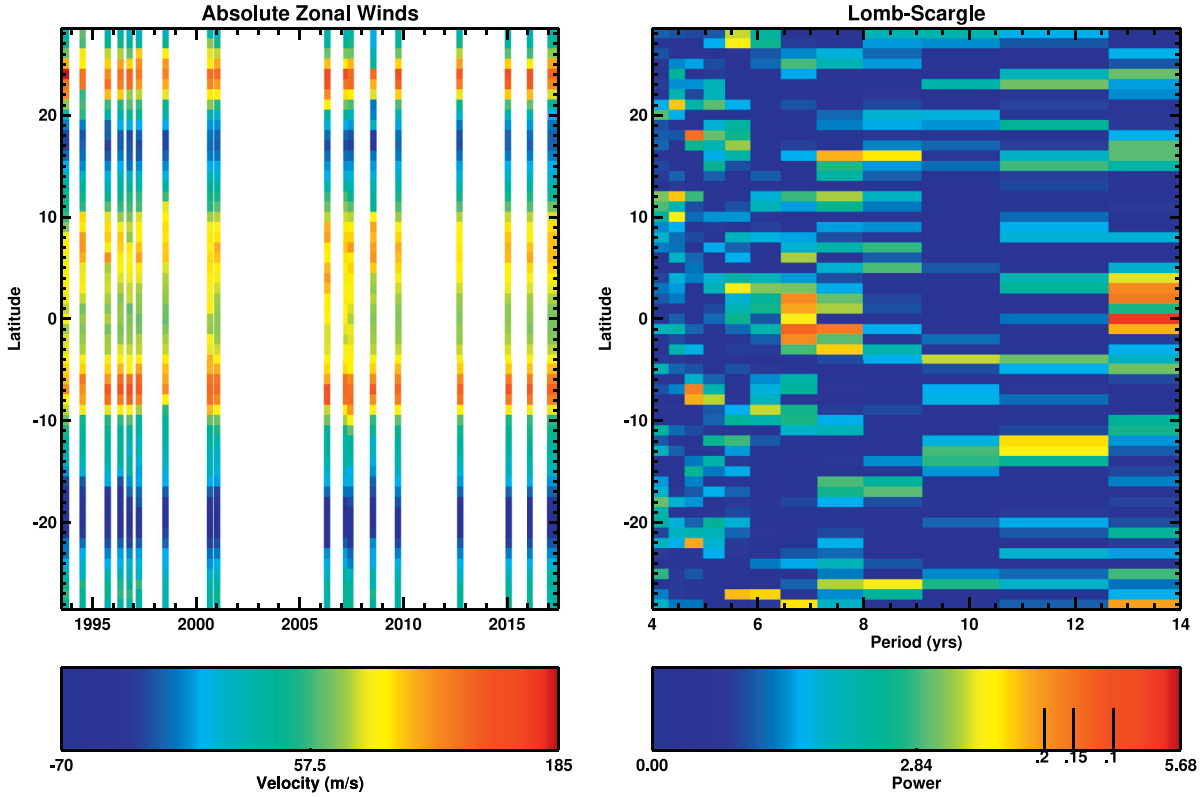

Fig. 10. Left: Time series of low-latitude zonal winds from WFC3 (2009–2016), combined with zonal winds measured from Voyager (not shown) and HST/WFPC2 data (Simon-Miller and Gierasch, 2010), with speeds corresponding to color values. Right: Corresponding Lomb-Scargle periodogram. False alarm probabilities of 20%, 15% and 10% are shown as vertical ticks on the color bar. The periodogram color bars span over the derived period mid-points, and correspond to periods of 4.2, 4.5, 4.8. 5.2, 5.6, 6.1, 6.7, 7.5, 8.5, 9.7, 11.4 and 13.8 yrs. (For interpretation of the references to color in this figure legend, the reader is referred to the web version of this article.)

A chain of such features, marked "Cyclone Alley" in Fig. 6, results in locally high mean zonal wind uncertainties near 55°S. These locally high uncertainties produce noticeable protrusions in the red envelopes in Figs. 7–9 near 55°S. Cyclone Alley in our velocity residual maps coincides with where the Galileo imaging experiment found the highest density of lightning strikes per unit area (Little et al., 1999; 52.5°S planetocentric latitude in their Table 2 is equivalent to 56.1°S planetographic latitude in our figures). Cyclones can be bordered by turbulent regions around their main bodies (resulting in 'frilly' looking structures). Levin et al. (1983) concluded that water cloud particles are the most likely medium for Jupiter's lightning generation, based on estimates of electrical conductivity for the different jovian cloud materials, as well as mass loading values that are consistent with values in more recent work by Wong et al. (2015a). Thus, evidence of cyclones and lightning near 55°S suggests that the vortices could vertically extend to pressures associated with the water cloud layer between 5–8 bar (Weidenschilling and Lewis, 1973; Wong et al., 2008; Bjoraker et al., 2015).

The large, turbulent, convectively active region to the northwest of the GRS (the "GRS wake") displays a consistent signature in the velocity residuals, at all epochs. The residual wind blows to the northwest in the northern section of the GRS wake, and to the southeast in the southern section, and thus corresponds to divergent flow at the cloud top level. Although divergent flow has been known to characterize individual convective supercells in this region, which themselves generate both cyclonic and anticyclonic eddies (Gierasch et al., 2000), our residual maps indicate that the entire region is characterized by large-scale divergence.

A persistent feature in the ZWPs at the same latitude as the GRS wake (within the SEB) is a "kink" in the meridional wind shear in the 10°–15°S range. It might seem plausible that the kink may be associated with the GRS wake, since its velocity residual is so large. The 2009 and 2012 two-hemisphere analyses test this hypothesis, since at each epoch, the GRS wake was present in only one of the hemispheres. Indeed, for 2012, significant differences (15–18 ms^{-1}) are present around the kink (Fig. 8). The kink is much weaker (smaller changes in meridional shear) in the hemisphere that does contain the GRS wake.

For 2009, a significant difference is not seen, consistent with the absence of a turbulent GRS wake at that time; convective activity had stopped and the SEB was quiescent and whitening (Fletcher et al., 2011). Conversely in 2008, the wind speed in the kink was particularly slow, and convective activity was present at most longitudes at this time (see Fig. 1 of Asay-Davis et al. (2011)). There seems to be a correlation between large-scale convective activity and slower zonal wind speeds near 10–15°S. One caveat is that gaps in the temporal sampling of our 2009 dataset degraded the sensitivity to velocities near 270°W, just to the west of the GRS (Supplemental Fig. S1, Velocity Residuals for 2009).

An additional velocity feature is present at these latitudes for the 2016.11 data, but not for any other epoch. This feature consists of a diagonal streak of eastward velocity residuals (Fig. 6) that corresponds to a thin, zone-like linear cloud feature in the albedo map (Fig. 4). Longitudinally, the velocity residual feature and the albedo feature both alternate in sign, with one complete cycle around the planet (zonal wavenumber 1), possibly an example of the GRS and its turbulent wake reflecting large-scale waves back toward the equator (Simon-Miller et al., 2012). When similar albedo features are present (2009 and 2016.95 epochs), they maintain a simlar slope in latitude/longitude, yet the velocity residual features appear to be aligned strictly east-west. This may be an ef-

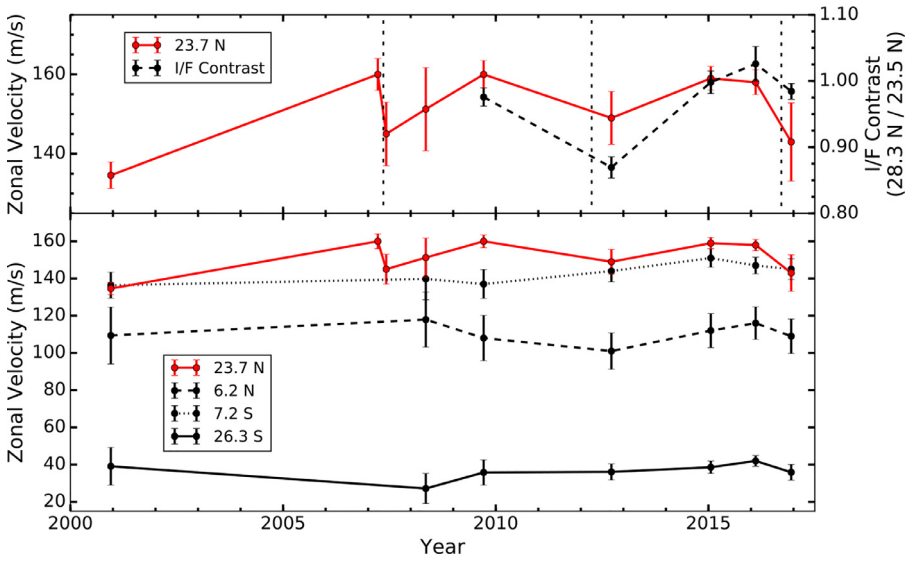

Fig. 11. Bottom: Equatorial jet peak velocities (ms^{-1}) vs. year. Top: 24N jet peak velocities (solid red line) and I/F contrast (dashed black line) vs. year. Vertical dashed lines indicate the time of an NTB plume outbreak. (For interpretation of the references to color in this figure legend, the reader is referred to the web version of this article.)

fect of the much coarser resolution of velocity residual maps compared to albedo maps. The planetary-scale linear albedo feature may be at a different altitude than the surrounding clouds, but the feature is much weaker in CH_4-band (889-nm) images than in the deep-sensing red wavelengths used in this study. The nature of this feature, and its corresponding velocity residuals, remains elusive.

Velocity fields derived from HST/WFC3 observations will provide valuable comparisons with a wide range of observations taken by the NASA *Juno* spacecraft, as well as other supporting observations from the ground. In particular, JunoCam will measure winds in some polar images with time separations on the order of an hour, which could be directly cross-validated with our wind profiles if the data extend to latitudes lower than 70°. Infrared global imaging sequences at 4.8 μm acquired by *Juno*'s JIRAM instrument can be used to measure the wind field with potential sensitivity to deeper tracers,[5] potentially revealing vertical wind shear in combination with data from HST. Repeated spacecraft passes over Jupiter at different longitudes will enable MWR, the Microwave Radiometer (Janssen et al., 2017), to sample deep composition in and out of discrete features such as the Great Red Spot and 5-μm hot spots. Horizontal wind fields from HST observations will complement the inferences on vertical motions derived from these MWR measurements. Ground-based stratospheric temperatures retrieved during the mission can be used to derive stratospheric winds via the thermal wind equation (Fletcher et al., 2016), using contemporaneous wind profiles as a lower boundary condition rather than wind fields measured over a decade before. Both the wind profiles and the optical maps themselves are also useful for comparison with spectrally-resolved microwave maps to be obtained during the *Juno* mission. These maps measure variability in NH_3 concentration, a tracer of vertical motion (de Pater et al., 2016).

5.3. Year-to-year differences

Fig. 11 plots our calculated year-to-year differences of Jupiter's equatorial jet peaks, including Cassini (Porco et al., 2003) and HST WFPC2 data (Asay-Davis et al., 2011). The long-term trend confirms that the jet peaks are stable (although they may vary significantly year-to-year). The most activity is seen at Jupiter's strong eastward jet at 24°N. This jet has been intensely studied over several decades and with a variety of instruments, including: the Voyager era (Maxworthy, 1984), ground based CCD and HST/WFPC2 images (García-Melendo et al., 2000) and most recently, from JunoCam and ground-based observations (Sánchez-Lavega et al., 2017). However, predicting the amplitude and period of variations in this jet peak has remained elusive to date. Fig. 12 plots the ZWP around the Northern Temperate Belt (NTB) jet peak for each epoch. The biggest decreases in jet speed follow eruptions of massive convective outbreaks, which result in a decrease from about 160 ms^{-1} to 147 ms^{-1} (Sánchez-Lavega et al., 2008). The jet peak also appeared to widen and slow by 50 ms^{-1} between the Voyager era and the period 1994–1997, which may be a result of 1990 disturbance in the NTB (García-Melendo et al., 2000). These outbreaks imply significant vertical wind shear between the visible cloud deck and deeper levels, with sporadic coupling of the layers driven by convective release of internal heat. Three such drops in the jet speed are shown in the top panel of Fig. 11: in 2007 after a well-documented convective outbreak in the North Temperate Belt (NTB), in 2012, and at the end of 2016. The 2012 speed drop followed another such outbreak that was very poorly imaged because it happened near solar conjunction (Rogers and Adamoli, 2012). The roughly 5-year interval between these events suggested a third possible event in 2017, but an outbreak was observed slightly earlier in October 2016 in infrared imaging by the NASA IRTF, shown in Fig. 13 and available for view at http://junoirtf.space.swri.edu (Rogers, 2016). The 2016.95 ZWP, acquired roughly two months after the onset of this latest outbreak, show another dramatic drop in jet speed, from 160 ms^{-1} to 144 ms^{-1}. The difference in the latitude of the NTB jet peaks in 2008 and 2016.11 are also modestly significant based on estimates of the uncertainty in the navigation procedure ($\sigma \sim 0.10°$ per frame).

The dissipation of NTB outbreaks is also associated with albedo changes in this region. The top panel of Fig. 11 shows the I/F contrast between the jet peak and the region directly to the north. There is a correlation between this contrast and the zonal velocity, with the 2012 jet speed drop correlated with a darkening of the NTB near 28°N. The darkening is also apparent comparing Fig. 2 to e.g., Fig. 1. This pattern is consistent with neutral, pre-plume conditions where the region is bright (seen from Voyager), followed by a chaotic disturbance and rapid darkening during and shortly after plume eruption observed via ground-based telescopes

[5] See https://photojournal.jpl.nasa.gov/catalog/PIA21036.

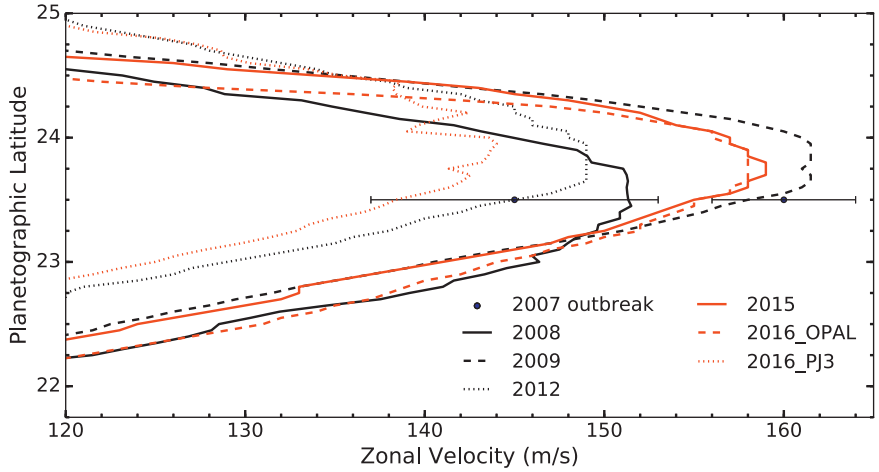

Fig. 12. Zoomed in ZWPs highlighting the changes in the NTB jet peak speed over the past decade. 2008–2012 data are shown in black lines and 2015–2016 data with red lines. The points from the 2007 plume outbreak come from Sánchez-Lavega et al. (2008). (For interpretation of the references to color in this figure legend, the reader is referred to the web version of this article.)

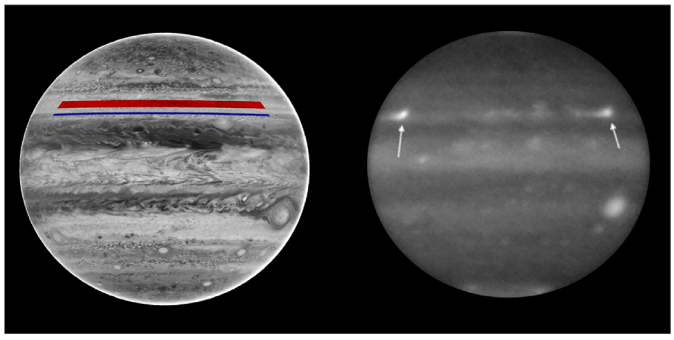

Fig. 13. Left: Image corrected for limb darkening shows area used to calculate the I/F contrast in Fig. 11; the red region is centered around 28.3°N and the blue around 23.5°N. Right: Near-infrared image of the NTB plume outbreak on 19 Oct 2016, taken with SpeX (Rayner et al., 2003) at the NASA IRTF. Plumes are indicated with arrows. (For interpretation of the references to color in this figure legend, the reader is referred to the web version of this article.)

and HST (Sánchez-Lavega et al., 1991; 2008; 2017). Barrado-Izagirre et al. (2009) also monitored the brightness distribution as the 2007 NTB disturbance developed, verifying changes in the slope of the brightness power spectra as well as an increase in dark cloud patches post-plume that may be consistent with Rossby wave dispersion. However, the I/F contrast following the October 2016 plume outbreak only modestly decreased, suggesting that the response to the outbreak is more rapid in the velocity field than in the cloud albedo. An unprecedented high cadence of microwave observations, with *Juno*'s Microwave Radiometer (Janssen et al., 2017) and ground-based VLA data (de Pater et al., 2016), will help determine whether there are also sub-cloud changes in volatile concentrations before and after the 2016 outbreak.

The South Temperate Belt (STB) also exhibits significant ZWP variations between some epochs. Fig. 14 plots the STB ZWP for each epoch. The variation in this region consists mainly in the presence or absence of a sub-peak at 29°S, and we find that it appears to correlate with the presence of a dark STB segment at 29–32°S. The 29°S sub-peak was present in 2008, 2009, and 2012 (hemisphere A), where such a STB segment was present, and not in 2012 (hemisphere B) nor 2016, where the STB segment was absent. In 2015, the 29°S sub-peak was not visible in the global ZWP, despite the presence of a short STB segment 19° long just west of oval BA; however, the map of residuals (see Supplemental Materials Figs. S3, velocity residuals for 2015) shows a strong eastward anomaly at 29°S precisely alongside this segment (and indeed, rapid circulation around the segment). These results confirm the report of Rogers et al. (2013), who likewise inferred that the 29°S sub-peak was conspicuous only in sectors containing a dark STB segment, from both HST and ground-based data in 2009

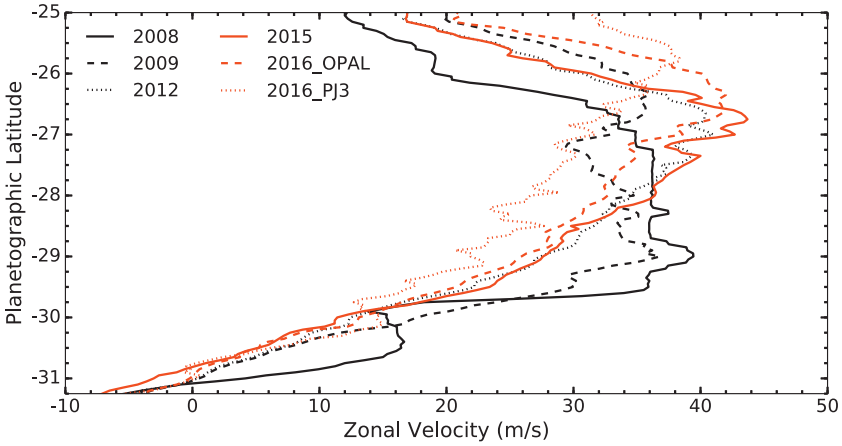

Fig. 14. As Fig. 12 but zoomed over the STB.

and 2012. Methods which do not smear the longitudinal velocity should be considered when determining the true flow in the STB region.

6. Conclusion

We present five epochs of WFC3 HST Jupiter observations and zonal wind analysis from 2009–2016. We used the 1D correlation method for velocity extraction (Asay-Davis et al., 2011). The derived 2016 zonal wind fields are the most timely for comparison to NASA *Juno* observations in late 2016 (PJ1 and PJ3).

We find that the zonal winds are globally stable on Jupiter throughout these epochs with some exceptions. The largest uncertainty in the wind field is found to be when vortices or hot spots are present. These phenomena do not follow the background flow, and thus increase the uncertainty of the extracted zonal velocity. This agrees with analysis from Asay-Davis et al. (2011). Vortices with the strongest deviations from the mean flow can be identified in our residual maps (Fig. 6) as paired N/S or E/W velocities. Future studies of Jupiter's zonal winds may construct similar maps to identify vortex features, including global Rossby waves resulting from vortex dynamics.

By deriving zonal winds from subsets of data—interleaved or covering only single hemispheres rather than all longitudes—we are able to isolate longitudinal variability as the dominant source of uncertainty in zonal wind retrievals. WFC3's slightly finer pixel scale and larger field of view, compared to WFPC2, result in a roughly factor of two reduction (from 10 ms^{-1} to 5–6 ms^{-1}) in uncertainty over our previous HST-based wind profile calculated with the same methods from Asay-Davis et al. (2011).

We also find variations in the 24°N jet peak velocity from 2009–2012. Specifically, the 2012 jet peak velocity is about 10 ms^{-1} slower than the 2009 and 2015 velocities. A 2012 plume outbreak, while not directly observed, is consistent with global changes to the albedo in the NTB. Brightness and velocity variations pre- and post-plume outbreak were also seen during other plume outbreaks on Jupiter (Sánchez-Lavega et al., 1991; 2008). A recent plume outbreak was observed in late 2016 with IRTF. Continued monitoring of the NTB with *Juno*'s Microwave Radiometer, ground-based telescopes, and amateur observations will be crucial for understanding the workings of these highly energetic storms, and their role in coupling the visible cloud deck with deeper atmospheric layers.

Acknowledgments

Based on observations made with the NASA/ESA Hubble Space Telescope, obtained from the Data Archive at the Space Telescope Science Institute, which is operated by the Association of Universities for Research in Astronomy, Inc., under NASA contract NAS 5-26555. These observations are associated with programs listed in Table 2. Support for programs 11559, 13937, 14334, and 14661 was provided by NASA through a grant from the Space Telescope Science Institute. This work has also been supported in part by NASA under the NASA Earth and Space Science Fellowship program Grant NNX16AP12H to UC Berkeley. For observations shown in Fig. 13, the authors thank Tom Momary, Tommy Greathouse, and Leigh Fletcher, Visiting Astronomers at the Infrared Telescope Facility, which is operated by the University of Hawaii under contract NNH14CK55B with NASA. The authors wish to recognize and acknowledge the very significant cultural role and reverence that the summit of Mauna Kea has always had within the indigenous Hawaiian community. We are most fortunate to have the opportunity to conduct observations from this mountain.

Supplementary materials

Supplementary data associated with this article can be found, in the online version, at 10.1016/j.icarus.2017.06.007.

References

Arregi, J., Rojas, J.F., Sánchez-Lavega, A., Morgado, A., 2006. Phase dispersion relation of the 5-micron hot spot wave from a long-term study of Jupiter in the visible. J. Geophys. Res. 111, E09010. doi:10.1029/2005JE002653.

Asay-Davis, X.S., Marcus, P.S., Wong, M.H., de Pater, I., 2011. Changes in Jupiter's zonal velocity between 1979 and 2008. Icarus 211 (2), 1215–1232. doi:10.1016/j.icarus.2010.11.018.

Barrado-Izagirre, N., Pérez-Hoyos, S., García-Melendo, E., Sánchez-Lavega, A., 2009. Evolution of the cloud field and wind structure of jupiter's highest speed jet during a huge disturbance. Astron. Astrophys. 507 (1), 513–522. doi:10.1051/0004-6361/200912282.

Barrado-Izagirre, N., Rojas, J.F., Hueso, R., Sánchez-Lavega, A., Colas, F., Dauvergne, J.L., Peach, D., Team IOPW, 2013. Jupiter's zonal winds and their variability studied with small-size telescopes. Astron. Astrophys. 554, A74. doi:10.1051/0004-6361/201321201.

Bjoraker, G.L., Wong, M.H., de Pater, I., Ádámkovics, M., 2015. Jupiter's deep cloud structure revealed using keck observations of spectrally resolved line shapes. Astrophys. J. 810, 122. doi:10.1088/0004-637X/810/2/122. 1508.04795.

Bolton, S., Adriani, A., Adumitroaie, V., Anderson, J., Atreya, S., Bloxham, J., Brown, S., Connerney, J., DeJong, E., Folkner, W., Gautier, D., Gulkis, S., Guillot, T., Hansen, C., Hubbard, W., Iess, L., Ingersoll, A., Janssen, M., Jorgensen, J., Kaspi, Y., Levin, S., Li, C., Lunine, J., Miguel, Y., Orton, G., Owen, T., Ravine, M., Smith, E., Steffes, P., Stone, E., Stevenson, D., Thorne, R., Waite, J., 2017. Jupiter's interior and deep atmosphere: the first close polar pass with the Juno spacecraft. Science. In press.

Cheng, A.F., Simon-Miller, A.A., Weaver, H.A., Baines, K.H., Orton, G.S., Yanamandra-Fisher, P.A., Mousis, O., Pantin, E., Vanzi, L., Fletcher, L.N., Spencer, J.R., Stern, S.A., Clarke, J.T., Mutchler, M.J., Noll, K.S., 2008. Changing characteristics of Jupiter's little red spot. Astrophys. J. 135, 2446–2452. doi:10.1088/0004-6256/135/6/2446.

Choi, D.S., Showman, A.P., Vasavada, A.R., Simon-Miller, A.A., 2013. Meteorology of Jupiter's equatorial hot spots and plumes from Cassini. Icarus 223 (2), 832–843. doi:10.1016/j.icarus.2013.02.001.

Fincham, A., Delerce, G., 2000. Advanced optimization of correlation imaging velocimetry algorithms. Exp. Fluids 29 (1), S013–S022. doi:10.1007/s003480070003.

Fincham, A.M., Spedding, G.R., 1997. Low cost, high resolution DPIV for measurement of turbulent fluid flow. Exp. Fluids 23 (6), 449–462. doi:10.1007/s003480050135.

Fitzpatrick, P.J., de Pater, I., Luszcz-Cook, S., Wong, M.H., Hammel, H.B., 2014. Dispersion in Neptune's zonal wind velocities from NIR keck AO observations in july 2009. Astrophys. Space Sci. 350 (1), 65–88. doi:10.1007/s10509-013-1737-2.

Flasar, F.M., Kunde, V.G., Achterberg, R.K., Conrath, B.J., Simon-Miller, A.A., Nixon, C.A., Gierasch, P.J., Romani, P.N., Bézard, B., Irwin, P., Bjoraker, G.L., Brasunas, J.C., Jennings, D.E., Pearl, J.C., Smith, M.D., Orton, G.S., Spilker, L.J., Carlson, R., Calcutt, S.B., Read, P.L., Taylor, F.W., Parrish, P., Barucci, A., Courtin, R., Coustenis, A., Gautier, D., Lellouch, E., Marten, A., Prangé, R., Biraud, Y., Fouchet, T., Ferrari, C., Owen, T.C., Abbas, M.M., Samuelson, R.E., Raulin, F., Ade, P., Césarsky, C.J., Grossman, K.U., Coradini, A., 2004. An intense stratospheric jet on Jupiter. Nature 427, 132–135. doi:10.1038/nature02142.

Fletcher, L.N., Greathouse, T.K., Orton, G.S., Sinclair, J.A., Giles, R.S., Irwin, P.G.J., Encrenaz, T., 2016. Mid-infrared mapping of Jupiter's temperatures, aerosol opacity and chemical distributions with IRTF/TEXES. Icarus 278, 128–161. doi:10.1016/j.icarus.2016.06.008.

Fletcher, L.N., Orton, G.S., Rogers, J.H., Simon-Miller, A.A., de Pater, I., Wong, M.H., Mousis, O., Irwin, P.G.J., Jacquesson, M., Yanamandra-Fisher, P.A., 2011. Jovian temperature and cloud variability during the 2009–2010 fade of the south equatorial belt. Icarus 213, 564–580. doi:10.1016/j.icarus.2011.03.007.

García-Melendo, E., Arregi, J., Rojas, J.F., Hueso, R., Barrado-Izagirre, N., Gómez-Forrellad, J.M., Pérez-Hoyos, S., Sanz-Requena, J.F., Sánchez-Lavega, A., 2011. Dynamics of Jupiter's equatorial region at cloud top level from Cassini and HST images. Icarus 211, 1242–1257. doi:10.1016/j.icarus.2010.11.020.

García-Melendo, E., Sánchez-Lavega, A., 2001. A study of the stability of Jovian zonal winds from HST images: 1995–2000. Icarus 152 (2), 316–330. doi:10.1006/icar.2001.6646.

García-Melendo, E., Sánchez-Lavega, A., Gómez, J.M., Lecacheux, J., Colas, F., Miyazaki, I., Parker, D., 2000. Long-lived vortices and profile changes in the 23.7 N high-speed Jovian jet. Icarus 146, 514–524. doi:10.1006/icar.2000.6411.

Gierasch, P.J., Ingersoll, A.P., Banfield, D., Ewald, S.P., Helfenstein, P., Simon-Miller, A., Vasavada, A., Breneman, H.H., Senske, D.A., Galileo Imaging Team, 2000. Observation of moist convection in Jupiter's atmosphere. Nature 403, 628–630. doi:10.1038/35001017.

Gierasch, P.J., Magalhaes, J.A., Conrath, B.J., 1986. Zonal mean properties of Jupiter's upper troposphere from Voyager infrared observations. Icarus 67, 456–483. doi:10.1016/0019-1035(86)90125-9.

Hilbert, B., 2009. WFC3 SMOV Program 11427: UVIS Channel Shutter Shading. Technical Report.

Hueso, R., Sánchez-Lavega, A., Iñurrigarro, P., Rojas, J.F., Mendikoa, I., Gómez-Forrellad, J.M., Go, C., Peach, D., Colas, F., Vendovato, M., 2017. Jupiter cloud morphology and zonal winds from groundbased observations before and during Junos first perijove. Geophys. Res. Lett.. In Press.

Ingersoll, A.P., Beebe, R.F., Mitchell, J.L., Garneau, G.W., Yagi, G.M., Mller, J.-P., 1981. Interaction of eddies and mean zonal flow on Jupiter as inferred from Voyager 1 and 2 images. J. Geophys. Res. 86 (A10), 8733–8743. doi:10.1029/JA086iA10p08733.

Ingersoll, A.P., Dowling, T.E., Gierasch, P.J., Orton, G.S., Read, P.L., Sánchez-Lavega, A., Showman, A.P., Simon-Miller, A.A., Vasavada, A.R., 2004. Dynamics of Jupiter's atmosphere, pp. 105–128.

Irwin, P.G.J., Wong, M.H., Simon, A.A., Orton, G.S., Toledo, D., 2017. HST/WFC3 observations of Uranus' 2014 storm clouds and comparison with VLT/SINFONI and IRTF/SpeX observations. Icarus 288, 99–119.

Janssen, M., Oswald, J., Brown, S., Gulkis, S., Levin, S., Bolton, S., Allison, M., Atreya, S., D.Gautier, Ingersoll, A., Lunine, J., Orton, G., Owen, T., Steffes, P., Adumitroaie, V., Bellotti, A., Jewell, L., Li, C., Li, L., Misra, S., Oyafuso, F., Santos-Costa, D., Sarkissian, E., Williamson, R., Arballo, J., Kitiyakara, A., Chen, J., Maiwald, F., Larson, A., Pingree, P., Lee, K., Mazer, A., Redick, R., Hughes, R., Bedrosian, G., Dawson, D., Hatch, W., Russel, D., Chamberlain, N., Zawadski, M., Khayatian, B., Franklin, B., Conley, H., Kempenaar, J., Loo, M., Sunada, E., Wang, C., 2017. MWR: microwave radiometer for the Juno mission to Jupiter. Space Sci. Rev.. (in Press).

Johnson, P.E., Morales-Juberías, R., Simon, A., Gaulme, P., Wong, M.H., Cosentino, R.G., 2017. Longitudinal variability in Jupiter's zonal winds derived from multi-wavelength HST observations. Planet. Space Sci. submitted.

Karalidi, T., Apai, D., Schneider, G., Hanson, J.R., Pasachoff, J.M., 2015. Aeolus: a Markov chain Monte Carlo code for mapping ultracool atmospheres. An application on Jupiter and brown dwarf HST light curves. Astrophys. J. 814, 65. doi:10.1088/0004-637X/814/1/65. 1510.04251.

Kozhurina-Platais, V., 2014. Astrometric Correction for WFC3/UVIS Filter-Dependent Component of Distortion. Baltimore: STScI.

Leovy, C.B., Friedson, A.J., Orton, G.S., 1991. The quasiquadrennial oscillation of Jupiter's equatorial stratosphere. Nature 354, 380–382. doi:10.1038/354380a0.

Levin, Z., Borucki, W.J., Toon, O.B., 1983. Lightning generation in planetary atmospheres. Icarus 56, 80–115. doi:10.1016/0019-1035(83)90129-X.

Li, L., Ingersoll, A.P., Vasavada, A.R., Porco, C.C., Del Genio, A.D., Ewald, S.P., 2004. Life cycles of spots on Jupiter from Cassini images. Icarus 172, 9–23. doi:10.1016/j.icarus.2003.10.015.

Li, L., Ingersoll, A.P., Vasavada, A.R., Simon-Miller, A.A., Del Genio, A.D., Ewald, S.P., Porco, C.C., West, R.A., 2006. Vertical wind shear on Jupiter from Cassini images. J. Geophys. Res. 111 (E4). doi:10.1029/2005JE002556. n/a–n/a, E04004.

Lii, P.S., Wong, M.H., de Pater, I., 2010. Temporal variation of the tropospheric cloud and haze in the Jovian equatorial zone. Icarus 209 (2), 591–601. doi:10.1016/j.icarus.2010.05.021.

Limaye, S.S., 1986. Jupiter - new estimates of the mean zonal flow at the cloud level. Icarus 65, 335–352. doi:10.1016/0019-1035(86)90142-9.

Limaye, S.S., 1989. Jupiter: short-term variations of the mean zonal flow at the cloud level. NASA Sp. Publ. 494, 317–323.

Limaye, S.S., Revercomb, H.E., Sromovsky, L.A., Krauss, R.J., Santek, D.A., Suomi, V.E., Collins, S.A., Avis, C.C., 1982. Jovian winds from Voyager 2. Part I: zonal mean circulation. J. Atmos. Sci. 39 (7), 1413–1432. doi:10.1175/1520-0469(1982)039(1413:JWFVPI)2.0.CO;2.

Limaye, S.S., Sromovsky, L.A., 1991. Winds of Neptune: voyager observations of cloud motions. J. Geophys. Res. 96 (S01), 18941–18960. doi:10.1029/91JA01701.

Little, B., Anger, C.D., Ingersoll, A.P., Vasavada, A.R., Senske, D.A., Breneman, H.H., Borucki, W.J., The Galileo SSI Team, 1999. Galileo images of lightning on Jupiter. Icarus 142, 306–323. doi:10.1006/icar.1999.6195.

Martin, S.C., de Pater, I., Marcus, P., 2012. Neptune's zonal winds from near-IR Keck adaptive optics imaging in August 2001. Astrophys. Space Sci. 337 (1), 65–78. doi:10.1007/s10509-011-0847-y.

Maxworthy, T., 1984. The dynamics of a high-speed Jovian jet. Planet. Space Sci. 32 (8), 1053–1058. doi:10.1016/0032-0633(84)90062-X.

McMaster, B., et al., 2008. WFPC2 Instrument Handbook. Baltimore: STScI.

Ortiz, J.L., Orton, G.S., Friedson, A.J., Stewart, S.T., Fisher, B.M., Spencer, J.R., 1998. Evolution and persistence of 5-m hot spots at the galileo probe entry latitude. J. Geophys. Res. 103 (E10), 23051–23069. doi:10.1029/98JE00696.

Pasachoff, J.M., Schneider, G., Babcock, B.A., Lu, M., Edelman, E., Reardon, K., Widemann, T., Tanga, P., Dantowitz, R., Silverstone, M.D., Ehrenreich, D., Vidal-Madjar, A., Nicholson, P.D., Willson, R.C., Kopp, G.A., Yurchyshyn, V.B., Sterling, A.C., Scherrer, P.H., Schou, J., Golub, L., McCauley, P., Reeves, K., 2013. Three 2012 transits of Venus: from Earth, Jupiter, and Saturn. In: American Astronomical Society Meeting Abstracts #221. In: American Astronomical Society Meeting Abstracts, 221, p. 315.06.

de Pater, I., Sault, R.J., Butler, B., DeBoer, D., Wong, M.H., 2016. Peering through Jupiter's clouds with radio spectral imaging. Science 352 (6290), 1198–1201. doi:10.1126/science.aaf2210. http://science.sciencemag.org/content/352/6290/1198.full.pdf

Pérez-Hoyos, S., Sánchez-Lavega, A., 2006. On the vertical wind shear of Saturn's equatorial jet at cloud level. Icarus 180, 161–175. doi:10.1016/j.icarus.2005.07.011.

Porco, C.C., West, R.A., McEwen, A., Del Genio, A.D., Ingersoll, A.P., Thomas, P., Squyres, S., Dones, L., Murray, C.D., Johnson, T.V., Burns, J.A., Brahic, A., Neukum, G., Veverka, J., Barbara, J.M., Denk, T., Evans, M., Ferrier, J.J., Geissler, P., Helfenstein, P., Roatsch, T., Throop, H., Tiscareno, M., Vasavada, A.R., 2003. Cassini imaging of Jupiter's atmosphere, satellites, and rings. Science 299 (5612), 1541–1547. doi:10.1126/science.1079462. http://science.sciencemag.org/content/299/5612/1541.full.pdf.

Rayner, J.T., Toomey, D.W., Onaka, P.M., Denault, A.J., Stahlberger, W.E., Vacca, W.D., Cushing, M.C., Wang, S., 2003. Spex: a medium-resolution 0.8–5.5 micron spectrograph and imager for the NASA infrared telescope facility. Publ. Astron. Soc. Pac. 115, 362–382. doi:10.1086/367745.

Rogers, J., 2016. Jupiter in 2016/17: Report no.1. First report on the 2016 NTBs outbreak. British Astronomical Association.

Rogers, J., Adamoli, G., 2012. Jupiter in 2012/13: Interim report no.3 (2012 Sep.20) Progress of Jupiters Great northern upheaval. British Astronomical Association.

Rogers, J., Adamoli, G., Hahn, G., Jacquesson, M., Vedovato, M., Mettig, H.J., 2013. Jupiters South Temperate Domain: Behaviour of Long-Lived Features and Jets, 2001-2012.. British Astronomical Association.

Sánchez-Lavega, A., García-Melendo, E., Pérez-Hoyos, S., Hueso, R., Wong, M.H., Simon, A., Sanz-Requena, J.F., Antuñano, A., Barrado-Izagirre, N., Garate-Lopez, I., Rojas, J.F., Del Río-Gaztelurrutia, T., Gómez-Forrellad, J.M., de Pater, I., Li, L., Barry, T., 2016. An enduring rapidly moving storm as a guide to Saturn's equatorial jet's complex structure. Nat. Commun. 7, 13262. doi:10.1038/ncomms13262.

Sánchez-Lavega, A., Miyazaki, I., Parker, D., Laques, P., Lecacheux, J., 1991. A disturbance in Jupiter's high-speed North temperate jet during 1990. Icarus 94 (1), 92–97. doi:10.1016/0019-1035(91)90142-G.

Sánchez-Lavega, A., Orton, G.S., Hueso, R., Garcia-Melendo, E., Perez-Hoyos, S., Simon-Miller, A., Rojas, J.F., Gomez, J.M., Yanamandra-Fisher, P., Fletcher, L., Joels, J., Kemerer, J., Hora, J., Karkoschka, E., de Pater, I., Wong, M.H., Marcus, P.S., Pinilla-Alonso, N., Carvalho, F., Go, C., Parker, D., Salway, M., Valimberti, M., Wesley, A., Pujic, Z., 2008. Depth of a strong jovian jet from a planetary-scale disturbance driven by storms. Nature 451 (7177), 437–440.

Sánchez-Lavega, A., Rogers, J.H., Orton., S.G., García-Melendo, E., Legarreta, J., Colas, F., Dauvergne, J.L., Hueso, R., Rojas, J.F., Pérez-Hoyos, S., Mendikoa, I., Iñurrigarro, P., Gómez-Forrellad, J.M., Momary, T., Hansen, C.J., Eichstaedt, G., Miles, P., Wesley, A., 2017. A planetary-scale disturbance in the most intense Jovian atmospheric jet from 2 JunoCam and ground-based observations. Geophys. Res. Lett.. In Press.

Simon, A.A., Wong, M.H., Orton, G.S., 2015. First results from the Hubble OPAL program: Jupiter in 2015. Astrophys. J. 812 (1), 55.

Simon-Miller, A.A., Gierasch, P.J., 2010. On the long-term variability of Jupiter's winds and brightness as observed from Hubble. Icarus 210, 258–269. doi:10.1016/j.icarus.2010.06.020.

Simon-Miller, A.A., Poston, B.W., Orton, G.S., Fisher, B., 2007. Wind variations in Jupiter's equatorial atmosphere: a QQO counterpart? Icarus 186, 192–203. doi:10.1016/j.icarus.2006.08.009.

Simon-Miller, A.A., Rogers, J.H., Gierasch, P.J., Choi, D., Allison, M.D., Adamoli, G., Mettig, H.-J., 2012. Longitudinal variation and waves in Jupiter's south equatorial wind jet. Icarus 218, 817–830. doi:10.1016/j.icarus.2012.01.022.

Sromovsky, L.A., Limaye, S.S., Fry, P.M., 1993. Dynamics of Neptune's major cloud features. Icarus 105, 110–141. doi:10.1006/icar.1993.1114.

Tollefson, J., de Pater, I., Marcus, P.S., Luszcz-Cook, S., Sromovsky, L.A., Fry, P.M., Fletcher, L.N., Wong, M.H., 2017. Vertical wind shear in Neptunes upper atmosphere explained with a modified thermal wind equation. Icarus. Submitted.

Weidenschilling, S.J., Lewis, J.S., 1973. Atmospheric and cloud structures of the Jovian planets. Icarus 20, 465–476. doi:10.1016/0019-1035(73)90019-5.

Wong, M.H., Atreya, S.K., Kuhn, W.R., Romani, P.N., Mihalka, K.M., 2015a. Fresh clouds: a parameterized updraft method for calculating cloud densities in one-dimensional models. Icarus 245, 273–281. doi:10.1016/j.icarus.2014.09.042.

Wong, M.H., Fry, P.M., Simon, A.A., 2016. Neptune. IAUC 4278.

Wong, M.H., Lunine, J.I., Atreya, S.K., Johnson, T., Mahaffy, P.R., Owen, T.C., Encrenaz, T., 2008. Oxygen and other volatiles in the giant planets and their satellites. Rev. Mineral. Geochem. 68, 219–246. doi:10.2138/rmg.2008.68.10.

Wong, M.H., Pavlosky, C., Long, K., et al., 2010. Wide Field Camera 3 Instrument Handbook. Baltimore: STScI.

Wong, M.H., Simon, A.A., Orton, G.S., de Pater, I., Sayanagi, K.M., 2015b. Hubble's long-term OPAL (outer planet atmospheres legacy) program observes cloud activity on Uranus. In: Lunar and Planetary Science Conference. In: Lunar and Planetary Institute, Technical Report, 46, p. 2606.